

1 Source attribution using FLEXPART and carbon monoxide 2 emission inventories: SOFT-IO version 1.0

3 Bastien Sauvage¹, Alain Fontaine¹, Sabine Eckhardt³, Antoine Auby⁴, Damien Boulanger²,
4 Hervé Petetin¹, Ronan Paugam⁵, Gilles Athier¹, Jean-Marc Cousin¹, Sabine Darras³, Philippe
5 Nédélec¹, Andreas Stohl³, Solène Turquety⁶, Jean-Pierre Cammas⁷ and Valérie Thouret¹.

6
7 ¹Laboratoire d'Aérologie, Université de Toulouse, CNRS, UPS, France

8 ²Observatoire Midi-Pyrénées, Toulouse, France

9 ³NILU - Norwegian Institute for Air Research, Kjeller, Norway

10 ⁴CAP HPI, Leeds, United Kingdom

11 ⁵King's College, London, United Kingdom

12 ⁶Laboratoire de Météorologie Dynamique/IPSL, UPMC Univ. Paris 6, Paris, France

13 ⁷Observatoire des Sciences de l'Univers de la Réunion (UMS 3365) et Laboratoire de l'Atmosphère et des
14 Cyclones (UMR 8105), Université de la Réunion, Saint-Denis, La Réunion, France

15
16
17 *Correspondence to:* Bastien Sauvage (bastien.sauvage@aero.obs-mip.fr)

18 **Abstract.** Since 1994, the In-service Aircraft for a Global Observing System (IAGOS) program has produced
19 in-situ measurements of the atmospheric composition during more than 51000 commercial flights. In order to
20 help analyzing these observations and understanding the processes driving the observed concentration
21 distribution and variability, we developed the SOFT-IO tool to quantify source/receptor links for all measured
22 data. Based on the FLEXPART particle dispersion model (Stohl et al., 2005), SOFT-IO simulates the
23 contributions of anthropogenic and biomass burning emissions from the ECCAD emission inventory database
24 for all locations and times corresponding to the measured carbon monoxide mixing ratios along each IAGOS
25 flight. Contributions are simulated from emissions occurring during the last 20 days before an observation,
26 separating individual contributions from the different source regions. The main goal is to supply added-value
27 products to the IAGOS database by evincing the geographical origin and emission sources driving the CO
28 enhancements observed in the troposphere and lower stratosphere. This requires a good match between observed
29 and modeled CO enhancements. Indeed, SOFT-IO detects more than 95% of the observed CO anomalies over
30 most of the regions sampled by IAGOS in the troposphere. In the majority of cases, SOFT-IO simulates CO
31 pollution plumes with biases lower than 10-15 ppbv. Differences between the model and observations are larger
32 for very low or very high observed CO values. The added-value products will help in the understanding of the
33 trace-gas distribution and seasonal variability. They are available in the IAGOS data base via
34 <http://www.iagos.org>. The SOFT-IO tool could also be applied to similar data sets of CO observations (e.g.
35 ground-based measurements, satellite observations). SOFT-IO could also be used for statistical validation as well
36 as for inter-comparisons of emission inventories using large amounts of data.

37 1 Introduction

38 Tropospheric pollution is a global problem caused mainly by natural or human-triggered biomass burning,
39 and anthropogenic emissions related to fossil fuel extraction and burning. Pollution plumes can be transported

40 quickly on a hemispheric scale (within at least 15 days) by large scale winds or, more slowly (Jacob, 1999),
41 between the two hemispheres (requiring more than 3 months). Global anthropogenic emissions are for some
42 species (CO₂) in constant increase (Boden et al., 2015). However, recent commitments of some countries to
43 reduce greenhouse gas emissions (e.g. over the U.S., U.S. EPA's Inventory of U.S. Greenhouse Gas Emissions
44 and Sinks, 1990-2013; <http://www.epa.gov/climatechange/ghgemissions/usinventoryreport.html>) seems to
45 induce a stalling in other global emissions (NO_x, SO₂ and Black Carbon, Stohl et al., 2015), except for some
46 regions (Brazil, Middle East India, China) where NO_x emissions increase (Miyazaki, 2017). In order to better
47 understand large-scale pollution transport, large amounts of in situ and space-based data have been collected in
48 the last three decades, allowing a better understanding of pollution variability and its connection with
49 atmospheric transport patterns (e.g. Liu et al., 2013). These data-sets are also useful to quantify global pollution
50 evolution with respect to the emissions trends described above.

51 Despite the availability of large trace gas data sets, the data interpretation remains difficult for the following
52 reasons: (1) the sampling mode does not correspond to an a priori defined scientific strategy, as opposed to data
53 collected during field campaigns; (2) the statistical analysis of the data can be complicated by the large number
54 of different sources contributing to the measured pollution, and an automated analysis of the contributions from
55 these different sources is required if, for instance, regional trends in emissions are to be investigated; (3) the
56 sheer size of some of the data sets can make the analysis rather challenging. Among the long-term pollution
57 measurement programs, the IAGOS airborne program (<http://www.iagos.org/>, formerly known as the
58 Measurement of OZone by Airbus In-service airCRAFT -MOZAIC- program) is the only one delivering in-situ
59 measurement data from the free troposphere. IAGOS provides regular global measurements of ozone (O₃) - since
60 1994 -, carbon monoxide (CO) - since 2002 -, and nitrogen oxides (NO_y) – for the period 2001-2005 - obtained
61 during more than 51000 commercial aircraft flights up to now, with substantial extent of the instrumented
62 aircraft recently. The analysis of the IAGOS database is also complicated by the fact that primary pollutants (CO
63 and part of NO_y) are emitted by multiple sources, while secondary compounds (O₃) are produced by
64 photochemical transformations of these pollutants, often most efficiently when pollutants from different sources
65 mix.

66 A common approach to separate the different sources influencing trace gas observations is based on the
67 determination of the air mass origins through Lagrangian modeling. This approach allows linking the emission
68 sources to the trace gas observations (e.g. Nédélec et al., 2005; Sauvage et al., 2005, 2006; Tressol et al. 2008;
69 Gressent et al. 2014; Clark et al., 2015; Yamasoe et al., 2015). Lagrangian modeling of the dispersion of
70 particles allows accounting efficiently for processes such as large-scale transport, turbulence and convection.
71 When coupled with emission inventories Lagrangian modeling of passive tracers allows for instance to
72 understand ozone anomalies (Cooper et al., 2006; Wen et al., 2012), to quantify the importance of lightning NO_x
73 emissions for tropospheric NO₂ columns measured from space (Beirle et al., 2006), to investigate the origins of
74 O₃ and CO over China (Ding et al., 2013), or to investigate the sources influencing the observed CO₂ over the
75 high northern latitudes (Vay et al., 2011).

76 To help analyzing a large data set such as the IAGOS observations, it is important to provide scientific users
77 a tool for characterizing air mass transport and emission sources. This study presents a methodology to
78 systematically establish a link between emissions sources (biomass burning and anthropogenic emissions) and
79 concentrations at the receptor locations. Since CO is a substance that is emitted by combustion sources (both

80 anthropogenic and biomass burning) and since CO has a lifetime of months in the troposphere (Logan et al.,
81 1981; Mauzerall et al., 1998), it is often used as a tracer for pollution transport (Staudt et al. 2001; Yashiro et al.,
82 2009; Barret et al., 2016). It is therefore convenient to follow past examples and use simulated CO source
83 contributions to gauge the influence of pollution sources on the measurements also with SOFT-IO. Our
84 methodology uses the FLEXPART Lagrangian particle dispersion model (Stohl et al., 2005) and emission
85 inventories from the ECCAD emission database (Granier et al., 2012) in order to quantify the influence of
86 emissions sources on the IAGOS CO measurements. The goal is to provide the scientific community with added
87 value products that will help them analyzing and interpreting the large number of IAGOS measurements. The
88 methodology is focused on the development of a scientific tool (SOFT-IO version 1.0) based on FLEXPART
89 particle dispersion model, that simulates the contributions of anthropogenic and biomass burning emissions for
90 IAGOS CO measurements. This tool, which has the benefit to be adaptable to multiple emission inventories
91 without re-running FLEXPART simulations, is described and then evaluated in the present study with the large
92 data-sets of IAGOS CO measurements. SOFT-IO could be in the future easily adapted and used to analyze other
93 datasets of trace gas measurements such as from ground based observations, sondes, aircraft campaigns or
94 satellite observations.

95 The methodology will be described in the next section, and then evaluated at the example of case studies of
96 pollution plumes observed by IAGOS aircraft. Further evaluation is performed through statistical analysis.
97 Finally we discuss the limitations of the methodology by estimating its sensitivity to different input data sets
98 (emission inventories, meteorological analyses).

99 **2. In-situ observations database: MOZAIC and IAGOS programs**

100 The MOZAIC program (Marengo et al., 1998) was initiated in 1993 by European scientists, aircraft
101 manufacturers and airlines to better understand the natural variability of the chemical composition of the
102 atmosphere and how it is changing under the influence of human activity, with particular interest in the impact of
103 aircraft exhaust. Between August 1994 and November 2014, MOZAIC performed airborne in-situ measurements
104 of ozone, water vapor, carbon monoxide, and total nitrogen oxides. The measurements are geolocated (latitude,
105 longitude and pressure) and come along with meteorological observations (wind direction and speed,
106 temperature). Data acquisition is performed automatically during round-trip international flights (ascent, descent
107 and cruise phases) from Europe to America, Africa, Middle East, and Asia (Fig. 1).

108 Based on the technical expertise of MOZAIC, the IAGOS program (Petzold et al., 2015, and references therein)
109 has taken over and provides observations since July 2011. The IAGOS data set still includes ozone, water vapor,
110 carbon monoxide, meteorological observations, and measurements of cloud droplets (number and size) are also
111 performed. Depending on optional additional instrumentation, measurements of nitrogen oxides, total nitrogen
112 oxides or, in the near-future, greenhouse gases (CO₂ and CH₄), or aerosols, will also be made.

113 Since 1994, the IAGOS-MOZAIC observations have created a big data set that is stored in a single database
114 holding data from more than 51000 flights. The data set can be used by the entire scientific community, allowing
115 studies of chemical and physical processes in the atmosphere, or validation of global chemistry transport models
116 and satellite retrievals. Most of the measurements have been collected in the upper troposphere and lower
117 stratosphere, between 9 and 12 km altitude, with 500 flights/ aircraft/ year on up to 7 aircraft up to now.

118

119 The MOZAIC and IAGOS data (called “IAGOS” from here on) used in this study are in-situ observations of CO
120 only, which is being measured regularly on every aircraft since 2002 with more than 30000 flights, using a
121 modified infrared filter correlation monitor (Nédélec et al., 2003; Nédélec et al., 2015). The accuracy of the CO
122 measurements has been estimated at (30 s response time) ± 5 ppb, or $\pm 5\%$.

123

124 Several case studies of CO pollution plumes (Table 1) using IAGOS data have been published, where model
125 simulations allowed attribution of the measured CO enhancements to anthropogenic or biomass burning
126 emissions, either measured in the boundary layer or in the free troposphere, following regional or synoptic-scale
127 transport (e.g. Nédélec et al., 2005; Tressol et al., 2008; Cammas et al., 2009; Elguindi et al., 2010). These case
128 studies are used here to better define the requirements for our methodology (meteorological analyses and
129 emission inventory inputs). Some of them are detailed and re-analyzed in Sect. 4.

130 **3. Estimation of carbon monoxide source regions: methodology**

131 To establish systematic source-receptor relationships for IAGOS observations of CO, the Lagrangian dispersion
132 model FLEXPART (Stohl et al., 1998, 2005; Stohl and Thomson, 1999) is run over the entire database.
133 Lagrangian dispersion models usually represent the differential advection better than global Eulerian models
134 (which do not well resolve intercontinental pollution transport; Eastham et al., 2017), at a significantly lower
135 computational cost. In particular, small-scale structures in the atmospheric composition can often be
136 reconstructed from large-scale global meteorological data, which makes model results comparable to high-
137 resolution in situ observations (Pisso et al., 2010). In the past, many studies (Nédélec et al., 2005 ; Tressol et
138 al.,2008; Cammas et al., 2009; Elguindi et al., 2010; Gressent et al., 2014) used FLEXPART to investigate
139 specific pollution events observed by the IAGOS aircraft. However, in these former case studies, the link
140 between sources and observations of pollution was guessed a priori. The transport model was then used to
141 validate the hypothesis. For example, in the Cammas et al. (2009) study, observations of high CO during summer
142 in the upper troposphere and lower stratosphere east of Canada were guessed to originate from biomass burning
143 over Canada as this region is often associated with pyro-convection whose intensity usually peaks in the
144 summer. This origin was confirmed by the model analysis. In general, the origin of the observed pollution cannot
145 be guessed a priori, especially when analyzing measurements from thousands of flights. Moreover, multiple
146 sources are most of the time involved when the observed pollution is the result of the mixing of polluted air
147 masses from different regions and source types.

148 CO is often used as a tracer to quantify the contributions of the different sources to the observed pollution
149 episodes. CO is emitted by both the combustion of fossil fuels and by biomass burning, and its photochemical
150 lifetime against OH attack is usually 1 to 2 months in the troposphere (Logan et al., 1981; Mauzerall et al.,
151 1998). Therefore it is possible to link elevated CO mixing ratios (with respect to its seasonally varying
152 hemispheric baseline) to pollution sources without simulating the atmospheric chemistry.

153 **3.1 Backward transport modeling**

154 Simulations were performed using the version 9 of FLEXPART, which is described in detail by Stohl et al.
155 (2005) (and references therein). The model was driven using wind fields from the European Centre for Medium-
156 Range Weather Forecast (ECMWF) 6-hourly operational analyses and 3-hour forecasts. The ECMWF data are

157 gridded with a $1^\circ \times 1^\circ$ horizontal resolution, and with a number of vertical levels increasing from 60 in 2002 to
158 137 since 2013. The model was also tested using higher horizontal resolution (0.5°), and with ECMWF ERA-
159 Interim reanalysis, as their horizontal and vertical resolution and model physics are homogeneous during the
160 whole period of IAGOS CO measurements. However, operational analyses were used for our standard set-up, as
161 the transport model reproduced CO better when using these data for several case studies of pollution transport,
162 especially for plumes located in the UT. Indeed, operational analyses provide a better vertical resolution since
163 2006 (91 levels until 2013, then 137 levels against 60 levels for ERA-Interim) and thus a better representation of
164 the vertical wind shear, and the underlying meteorological model is also more modern than the one used for
165 producing ERA-Interim. Vertical resolution is one of the critical factors for modeling such CO plumes with the
166 best precision in terms of location and intensity (Eastham and Jacob, 2017).

167 Using higher horizontal resolution for met-fields analyses and forecasts (0.5° vs 1°) showed no influence on the
168 simulated carbon monoxide, despite larger computational time and storage needs. We assume further
169 improvement can be obtained using even higher horizontal resolution (0.1°), but this was not feasible at this
170 stage and should be considered in the future.

171
172 In order to be able to represent the small-scale structures created by the wind shear and observed in many
173 IAGOS vertical profiles, the model is initialized along IAGOS flight tracks every 10 hPa during ascents and
174 descents, and every 0.5° in latitude and longitude at cruise altitude. This procedure leads to i model initialization
175 boxes along every flight track. For each i , 1000 particles are released. Indeed 1000 to 6000 particles are
176 suggested for correct simulations in similar studies based on sensitivity tests on particles number (Wen et al.,
177 2012; Ding et al., 2013). For instance, a Frankfurt (Germany) to Windhoek (Namibia) flight contains around 290
178 boxes (290000 particles) of initialization as a whole.

179 FLEXPART is set up for backward simulations (Seibert and Frank, 2004) from these boxes as described in Stohl
180 et al. (2003) and backward transport is computed for 20 days prior to the in-situ observation, which is sufficient
181 to consider hemispheric scale pollution transport in the mid-latitudes (Damoah et al., 2004; Stohl et al., 2002;
182 Cristofanelli et al., 2013). This duration is also expected to be longer than the usual lifetime of polluted plumes
183 in the free troposphere, i.e. the time when the concentration of pollutants in plumes is significantly larger than
184 the surrounding background. Indeed, the tropospheric mixing time scale has been estimated to be typically
185 shorter than 10 days (Good et al., 2003; Pisso et al., 2009). Therefore the model is expected to be able to link air
186 mass anomalies such as strong enhancements in CO to the source regions of emissions (Stohl et al., 2003). It is
187 important to note that we aim to simulate recent events of pollution explaining CO enhancements over the
188 background, but not to simulate the CO background which results from aged and well-mixed emissions.

189 The FLEXPART output is a residence time, as presented and discussed in Stohl et al. (2003). These data
190 represent the average time spent by the transported air masses in a grid cell, divided by the air density, and are
191 proportional to the sensitivity of the receptor mixing ratio to surface emissions. In our case, it is calculated for
192 every input point along the flight track, every day for $N_t = 20$ days backward in time, on a 1° longitude x 1°
193 latitude global grid with $N_z = 12$ vertical levels (every 1 km from 0 to 12 km, and 1 layer above 12 km).

194 Furthermore, the altitude of the 2 PVU potential vorticity level above or below the flight track is extracted from
195 the wind and temperature fields, in order to locate the CO observations above or below the dynamical tropopause
196 according to the approach of Thouret et al. (2006).

197 3.2 Emission inventories from the ECCAD project

198 The main goal of the Emissions of atmospheric Compounds & Compilation of Ancillary Data (ECCAD) project
199 (Granier et al., 2012) is to provide scientific and policy users with datasets of surface emissions of atmospheric
200 compounds and ancillary data, i.e. data required for estimating or quantifying surface emissions. All the emission
201 inventories and ancillary data provided by ECCAD are published in the scientific literature.

202 For the current study, we selected five CO emission inventories. Four of them are available at global scale
203 (MACCcity and EDGAR v4.2 for anthropogenic; GFED 4 and GFAS v1.2 -GFAS v1.0 for 2002- for fires) from
204 the ECCAD database and cover most of the IAGOS CO database presented here (2002 - 2013). The global scale
205 inventories have a $0.1^\circ \times 0.1^\circ$ to $0.5^\circ \times 0.5^\circ$ horizontal resolution. They are provided with daily, monthly or
206 yearly time resolution. They are listed in Table 2 along with the references describing them. The four global
207 inventories are used to study the model's performance and sensitivity in Sect. 5.

208 To further test the sensitivity to the emission inventories, we also used one regional inventory, which is expected
209 to provide a better representation of emissions in its region of interest than generic global inventories. The aim is
210 to test the ability of regional inventories in better representing simulated CO for specific case studies. The goal
211 of using regional dataset in this paper is only to evaluate the incidence of one of them respect to global emission
212 inventories, not to evaluate the incidence of all regional dataset. We have chosen ICARTT because of improved
213 results demonstrated in the representation of boreal biomass burning fires in some specific cases (Turquety et al.,
214 2016) as for example the one based on MOZAIC data by Elguindi et al., (2010). Global emission inventories are
215 the first choice to interpret quasi global coverage of the CO IAGOS measurements. In the future we plan to
216 include regional emission inventories for the study of specific events. For biomass burning, the International
217 Consortium for Atmospheric Research on Transport and Transformation (ICARTT) campaign's North American
218 emissions inventory developed by Turquety et al. (2007) for the summer of 2004 and provided at $1^\circ \times 1^\circ$
219 horizontal resolution was tested. It combines daily area burned data from forest services with the satellite data
220 used by global inventories, and uses a specific vegetation database, including burning of peat lands which
221 represent a significant contribution to the total emissions.

222 3.3 Coupling transport output with CO emissions

223 Calculating the recent contributions $C(i)$ (kg m^{-3}) of CO emissions for every one of the i model's initialization
224 points along the flight tracks requires three kinds of data:

- 225 • the residence time T_R (in seconds, gridded with $N_x = 360$ by $N_y = 180$ horizontal points, $N_z = 12$ vertical
226 levels, $N_t = 20$ days) from backward transport described in Sect. 3.1,
- 227 • CO surface emissions $E_{CO}(N_x, N_y, N_t)$ (in $\text{kg CO} / \text{m}^2 / \text{s}$)
- 228 • the injection profile $Inj(z)$ defining the fraction of pollutants diluted in the different vertical levels (with
229 Δz being the thickness, in meters) just after emissions, and defined according to three different
230 approaches (DENTENER, MIXED or APT) described in the next paragraph:

231

$$232 \text{(Eq. 1)} \quad C(i) = \sum_{t=1}^{N_t} \sum_{y=1}^{N_y} \sum_{x=1}^{N_x} \sum_{z=1}^{N_z} Inj(z) \frac{T_R(x, y, z, t, i) E_{CO}(x, y, t)}{\Delta z(z)}$$

233

234 In the case of anthropogenic emissions, CO is simply emitted into the first vertical layer of the residence time
235 grid ($\Delta Z= 1000\text{m}$).

236

237 For biomass burning emissions, in the tropics and mid latitudes regions, the lifting of biomass burning plumes is
238 usually due to small and large scale dynamical processes, such as turbulence in the boundary layer, deep
239 convection and frontal systems, which are usually represented by global meteorological models. At higher
240 latitudes, however, boreal fires can also be associated with pyro-convection and quick injection above the
241 planetary boundary layer, even if CO tends to be mostly released during smoldering. Pyro-convection plume
242 dynamics are often associated with small-scale processes that are not represented in global meteorological data
243 and emission inventories (Paugam et al 2016). In order to characterize the effect of these processes, we
244 implemented three methodologies to parameterize biomass injection height:

245 • the first one (named DENTENER) depends only on the latitude and uses constant homogeneous
246 injection profiles as defined by Dentener et al. (2006) , i.e. 0-1 km for the tropics [30S-30N] (see green
247 line in Fig 2), 0-2 km for the mid-latitudes [60S-30S, 30N-60N] (see blue line in Fig. 2) and 0-6 km for
248 the boreal regions [90S-60S, 60N-90N] (not shown in Fig. 2).

249 • the second named MIXED uses the same injection profiles as in DENTENER for the tropics and mid-
250 latitudes, but for the boreal forest, injection profiles are deduced from a lookup table computed with the
251 plume rise model PRMv2 presented in Paugam et al. (2015). Using PRMv2 runs for all fires from
252 different years of the Northern-American MODIS archive, three daily Fire Radiative Power (FRP)
253 classes (under 10 TJ/day, between 10 and 100 TJ/day, and over 100 TJ/day) were used to identify three
254 distinct injection height profiles (see brown, red, and black lines in Fig. 2). Although PRMv2 reflects
255 both effects of the fire intensity through the input of FRP and active fire size and effects of the local
256 atmospheric profile, here for sake of simplicity only FRP is used to classify the injection profile.
257 Furthermore, when applied to the IAGOS data set, the MIXED method uses equivalent daily FRP
258 estimated from the emitted CO fluxes given by the emission inventories as described in Kaiser et al.
259 (2012)

260 • the third method named hereafter APT uses homogeneous profile defined by the daily plume top
261 altitude as estimated for each 0.1×0.1 pixel of the GFAS v1.2 inventory available for 2003 to 2013
262 (Rémy et al. 2016, and http://www.gmes-atmosphere.eu/oper_info/global_nrt_data_access/gfas_ftp/).
263 As in the MIXED method, GFAS v1.2 is using the plume model PRMV2 from Paugam et al. (2015),
264 but here the model is run globally for every assimilated GFAS-FRP pixel.

265

266 **3.4 Automatic detection of CO anomalies**

267 For individual measurement cases, plumes of pollution can most of the time be identified by the human eye
268 using the observed CO mixing ratio time series or the CO vertical profiles. However, this is not feasible for a
269 database of tens of thousands of observation flights. In order to create statistics of the model's performance, we
270 need to systematically identify observed pollution plumes in the IAGOS database. The methodology to do this is
271 based on what has been previously done for the detection of layers in the MOZAIC database (Newell et al.,
272 1999; Thouret et al., 2000), along with more recent calculations of the CO background and CO percentiles define

273 for different regions along the IAGOS data set (Gressent et al., 2014). An example demonstrating the procedure,
 274 which is described below, is shown in Fig. 3.

275
 276 In a first step, the measurement time series along the flight track (number of measurements n_{TOT}) is separated
 277 into three parts:

- 278 1. Ascent and descent vertical profiles (n_{VP}) in the PBL (altitudes ranging from the ground to 2 km) and in
 279 the free troposphere (from 2 km to the top altitude of the vertical profiles),
- 280 2. measurements at cruising altitude in the upper troposphere (n_{UT}),
- 281 3. measurements in the lower stratosphere (n_{LS})

282 such that
$$n_{TOT} = n_{VP} + n_{UT} + n_{LS}$$

283 where n_{VP} , n_{UT} and n_{LS} are the number of measurements along tropospheric ascents and descents, and in the upper
 284 troposphere and lower stratosphere, respectively. A range of altitudes from the surface to a top altitude identifies
 285 vertical profiles. The top altitude is 75 hPa above the 2 pvu dynamical tropopause (Thouret et al., 2006) when
 286 the aircraft reaches/leaves cruising altitude (during ascent/descent). The PV is taken from the ECMWF
 287 operational analyses and evaluated at the aircraft position by FLEXPART. Observations made during the cruise
 288 phase are flagged as upper tropospheric if the aircraft is below the 2 pvu dynamical tropopause. If not,
 289 observations are considered as stratospheric and then are ignored in the rest of the paper. Although CO
 290 contributions are calculated also in the stratosphere, the present study focuses on tropospheric pollution only.

291
 292 In a second step, the CO background mixing ratio is determined for each tropospheric part (C_{VP_back} and C_{UT_back} ,
 293 see Fig. 3 for illustration) for the tropospheric vertical profiles and for the upper troposphere respectively. For
 294 tropospheric vertical profiles, the linear regression of CO mixing ratio versus altitude is calculated from 2 km to
 295 the top of the vertical profiles, to account for the usual decrease of background CO with altitude. Data below
 296 2 km are not used because high CO mixing ratios caused by fresh emissions are usually observed close to surface
 297 over continents. The slope a (in ppb m^{-1}) of the linear regression is used to determine the background so that
 298 $C_{VP_back} = aZ$. The background is removed from the C_{VP} tropospheric vertical profiles mixing ratio to obtain a
 299 residual CO mixing ratio C_{VP}^R (Eq. 2).

300 (Eq. 2):
$$C_{VP}^R = C_{VP} - C_{VP_back}$$

301
 302 For the upper troposphere, the CO background mixing ratio (C_{UT_back}) is determined using seasonal median
 303 values (over the entire IAGOS database) for the different regions of Figure 4. Note that this approach was not
 304 feasible for vertical profiles as for most of the visited airports there are not enough data to establish seasonal
 305 vertical profiles. As for the profiles, background values are subtracted from the UT data to obtain residual C_{UT}^R
 306 (Eq. 3):

307 (Eq. 3):
$$C_{UT}^R = C_{UT} - C_{UT_back}$$

308
 309 In a third step, CO anomalies C^A are determined for tropospheric vertical profiles (C_{VP}^A) and in the upper
 310 troposphere (C_{UT}^A). Residual C_{VP}^R and C_{UT}^R values are flagged as CO anomalies when these values exceed the
 311 third quartile (Q3) of the residual mixing ratio $C_{VP}^R(Q3)$ for vertical profiles, or the third quartile of the residual
 312 seasonal values $C_{UT_season}^R(Q3)$ in the different regions (Fig. 4) for the UT. Note that $C_{VP}^R(Q3)$ or $C_{UT_season}^R(Q3)$

313 needs to be higher than 5 ppb (the accuracy of the CO instrument; Nédélec et al., 2015) in order to consider an
314 anomaly:

315 (Eq. 4): $C^A_{VP} = C^R_{VP}$ if $C^R_{VP} > C^R_{VP}(Q3)$

316 (Eq. 5): $C^A_{UT} = C^R_{UT}$ if $C^R_{UT} > C^R_{UT_season}(Q3)$

317 In the examples shown in Fig. 3a and Fig. 3b, the red line represents CO anomalies.

318 With this algorithm CO plumes are automatically detected in the entire IAGOS database. For each identified
319 plume, minimum and maximum values of the date, latitude, longitude and altitude, as well as the CO mean and
320 maximum mixing ratio, are archived. These values are used for comparison with modeled CO values.

321

322 4. Selected case studies to evaluate CO emission inventories and SOFT-IO's performance

323 As described in Sect. 2, a number of case studies documented in the literature were selected from the IAGOS
324 database in order to get a first impression of the model's performance. These case studies have been chosen to
325 represent the different pollution situations that are often encountered in the troposphere in terms of emissions
326 (anthropogenic or biomass burning) and transport (at regional or synoptic scale, pyro-convection, deep
327 convection, frontal systems). Systematic evaluation of the model performance against emission inventories will
328 be presented in Sect. 5.

329 4.1 Anthropogenic emission inventories

330 Among the case studies listed in Table 1, four were selected in order to illustrate the evaluation of the inventories
331 used for anthropogenic emissions:

- 332 • Landing profiles over Hong Kong from 19th of July and 22nd of October 2005 were selected in order to
333 investigate specifically Asian anthropogenic emissions.
- 334 • During the 10th of March 2002 Frankfurt–Denver and 27th of November 2002 Dallas–Frankfurt flights,
335 IAGOS instruments observed enhanced CO plumes in the North Atlantic upper troposphere, also linked
336 to anthropogenic emissions.

337 Figure 5a shows the observed (black line) and simulated (colored lines) CO mixing ratios above Hong Kong
338 during 22nd of October 2005. Note that background is not simulated but estimated from the observations as
339 described in Sect.3.4 (blue line, C_{VP_back}). The dashed blue line represents the residual CO mixing ratio C^R_{VP} .
340 Observations show little variability in the free troposphere down to around 3 km. Strong pollution is observed
341 below, with + 300 ppb enhancement over the background on average between 0 and 3 km. Note that we do not
342 discuss CO enhancement above 3 km.

343 In agreement with C^R_{VP} , SOFT-IO simulates a strong CO enhancement in the lowest 3 km of the profile, caused
344 by fresh emissions. However, the simulated enhancement is less strong than the observed one, a feature that is
345 typical for this region, as we shall see later.

346 In addition to the CO mixing ratio, SOFT-IO calculates CO source contributions and geographical origins of the
347 modeled CO, respectively displayed in Fig. 5b and Fig. 5c (using the methodology described in Sec. 3.4) and
348 using here MACCity and GFAS v1.2 as example. For the geographical origin we use the same 14 regions as
349 defined for the GFED emissions (<http://www.globalfiredata.org/data.html>). Note that only the average of the
350 calculated CO is displayed for each anomaly (0-3km; 3.5-6km) in Fig. 5b and Fig. 5c.

351
352 Colored lines in Fig. 5a show the calculated CO using anthropogenic sources described by the two inventories
353 selected in Sect. 3.2, MACCity (green line) and EDGARv4.2 (yellow line), along the flight track. In both cases,
354 biomass burning emissions are described by GFASv1.2. Emissions from fires have negligible influence (less
355 than 3%) on this pollution event as depicted in Fig. 5b.

356 In the two simulations, the calculated CO mixing ratio is below 50 ppb in the free troposphere, as we do not
357 simulate background concentrations with SOFT-IO. CO enhancement around 4 to 6 km is overestimated by
358 SOFT-IO. CO above 6 km is not considered as an anomaly, as $C_{UT}^R < C_{UT_season}^R(Q3)$. Simulated mixing ratios in
359 the 0-2 km polluted layer are almost homogeneous, with values around 280 ppb using MACCity and around 160
360 ppb using EDGARv4.2. They are attributed to anthropogenic emissions (more than 97% of the simulated CO)
361 originating mostly from Central Asia with around 95% influence. In this regard, the CO simulated using
362 MACCity is in better agreement with the observed CO than the one obtained using EDGARv4.2. Indeed, using
363 MACCity, simulated CO reaches 90% of the observed enhancement (+ 300 ppb on average) over the background
364 (around 100 ppb), while for EDGARv4.2 the corresponding value is only 53%, indicating strong underestimation
365 of this event. The difference in the calculated CO using these two inventories is also consistent with the results
366 of Granier et al. (2011) who showed strong discrepancies in the Asian anthropogenic emissions in different
367 inventories.

368
369 Figure 6a shows the CO measurements at cruising altitude during a transatlantic flight between Frankfurt and
370 Denver on 10th of March 2002. The dashed blue line represents the residual CO C_{UT}^R . Observations indicate that
371 the aircraft encountered several polluted air masses with CO mixing ratios above 110 to 120 ppb, which are the
372 seasonal median CO values in the two regions visited by the aircraft, obtained from the IAGOS database (see
373 Gressent et al., 2014). Three pollution plumes are measured:

- 374 • around 100°W (around +10 ppb of CO enhancement on average): plume 1
- 375 • between 80°W and 50°W (+30 ppb of CO enhancement on average): plume 2
- 376 • between 0° and 10°E (+40 ppb of CO enhancement on average): plume 3.

377 These polluted air masses are surrounded by stratospheric air masses with CO values lower than 80-90 ppb. As
378 polluted air masses were sampled at an altitude of around 10 km, they are expected to be due to long-range
379 transport of pollutants.

380 The calculated CO is shown in Fig. 6a using MACCity (green line), EDGARv4.2 (yellow line) for anthropogenic
381 emissions and GFASv1.0 for biomass burning emissions. SOFT-IO estimates that these plumes are mostly
382 anthropogenic (representing 77% to 93% of the total simulated CO, Fig. 6b). Pollution mostly originates from
383 Central and South-East Asia, with strong contribution from North America (Fig. 6c) for plume 3.

384 SOFT-IO correctly locates the three observed polluted air masses with the two anthropogenic inventories. CO is
385 also correctly calculated using MACCity, with almost the same mixing ratios on average as the observed
386 enhancements in the three plumes. Using EDGARv4.2, only 2/3 of the observed CO enhancements intensity is
387 reproduced, except for plume #1 with better intensity results. We have already seen in the previous case study
388 that emissions in Asia may be underestimated, especially in the EDGARv4.2 inventory.

389 Similar comparisons were performed in the four case studies selected to estimate and validate the anthropogenic
390 emission inventories coupled with the FLEXPART model. Results are summarized in Table 3. For three of the

391 cases, SOFT-IO simulations showed a better agreement with observations when using MACCity than when
392 using EDGARv4.2. In the fourth case both inventories performed equally well. One reason for the better
393 performance of MACCity is the fact that it provides monthly information (Table 2).
394

395 **4.2 Biomass burning emission inventories**

396 In order to evaluate and choose biomass burning emission inventories, we have selected eleven case studies with
397 fire-induced plumes (Table 1). Seven of them focused on North-American biomass burning plumes observed in
398 the free troposphere above Europe (flights on 30th of June, 22nd and 23rd of July 2004) and in the upper
399 troposphere/lower stratosphere above the North Atlantic (29th of June 2004) (e.g. Elguindi et al., 2010; Cammas
400 et al., 2009). Two are related to the fires over Western Europe during the 2003 heat wave (Tressol et al. 2008).
401 The two last ones, on the 30th and 31st of July 2008, focused on biomass burning plumes observed in the ITCZ
402 region above Africa as described in a previous study (Sauvage et al., 2007a).

403 The three datasets selected to represent biomass burning emissions are based on different approaches: GFAS
404 v1.2 (Kaiser et al., 2012) and GFED 4 emissions (Giglio et al., 2013) are calculated daily. GFAS v1.2 presents
405 higher spatial resolution. The ICARTT campaign inventory (Turquety et al., 2007) was specifically designed for
406 North-American fires during the summer of 2004 with additional input from local forest services.

407 Figure 7a illustrates the calculated CO contributions for the different fire emission inventories for one of the case
408 studies, on 22nd of July 2004 above Paris. The observations (black line) show high levels of CO in an air mass in
409 the free troposphere between 3 and 6 km, with mixing ratios 140 ppb above the background (blue line) deduced
410 from measurements. This pollution was attributed to long-range transport of biomass burning emission in North
411 America by Elguindi et al. (2010). Outside of the plume, the CO concentration decreases with altitude, from
412 around 150 ppb near the ground, to 100 ppb background in the upper free troposphere. This last value
413 corresponds to the median CO seasonal value deduced from the IAGOS database (Gressent et al., 2014). CO is
414 not considered as an anomaly near the ground as $C_{UT}^R < C_{UT_season}^R(Q3)$.

415 SOFT-IO simulations were performed for this case using MACCity to represent anthropogenic emissions, and
416 GFAS v1.2 (green line), GFED 4 (yellow line), or the ICARTT campaign inventory (red line). Fire vertical
417 injection is realized using the MIXED approach for the three biomass burning inventories, in order to only
418 evaluate the impact of choosing different emission inventories. In the three simulations, contributions show two
419 peaks, one near the ground that is half due to local anthropogenic emissions and half due to contributions from
420 North American biomass burning and thus not considered in this discussion.

421 The second more intense peak, simulated in the free troposphere where the enhanced CO air masses were
422 sampled, is mostly caused by biomass burning emissions (87% of the total calculated CO, Fig. 7b), originating
423 from North-America (99% of the total enhanced CO). When calculated using the ICARTT campaign inventory,
424 the simulated CO enhancement reaches over 150 ppb, which is 10 ppb higher than the observed mixing ratio
425 above the background (+140 ppb), but only for the upper part of the plume.

426 When using global inventories, the simulated contribution peak reaches 70 ppb using GFASv1.2 and 100 ppb
427 using GFED4, which appears to underestimate the measured enhancement (+140 ppb) by up to 50% to 70%
428 respectively. This comparison demonstrates the large uncertainty in simulated CO caused by the emission

429 inventories, both in the case of biomass burning or anthropogenic emissions. For that reason we aim to provide
430 simulations with different global and regional inventories in for the IAGOS data set.

431 As the ICARTT campaign inventory was created using local observations in addition to satellite products, the
432 large difference in the simulated CO compared to the other inventories may in part be due to different
433 quantification of the total area burned (for GFED, GFAS using the FRP as constraint). Turquety et al. (2007)
434 also discussed the importance of peat land burning during that summer. They estimated that they contributed
435 more than a third of total CO emissions (11 Tg of the 30 Tg emitted during summer 2004).

436

437 Figure 8a shows CO mixing ratios as a function of latitude for a flight from Windhoek (Namibia) to Frankfurt
438 (Germany) in July 2008. Observations indicate that the aircraft flew through polluted air masses around the
439 equator (10°S to 10°N), with +100 (+125) ppb of CO on average (at the most) above the 90 ppb background
440 deduced from seasonal IAGOS mixing ratios over this region. Such CO enhancements have been attributed to
441 regional fires injected through ITCZ convection (Sauvage et al., 2007b).

442 The SOFT-IO simulations (colored lines in Fig. 8a) link these air masses mostly to recent biomass burning
443 (responsible for 68% of the total simulated CO, Fig. 8b) in South Africa (Fig. 8c). The calculated CO shows
444 similar features both with GFED4 (yellow line) and GFASv1.2 (green line). The simulation also captures well
445 the intensity variations of the different peaks: maximum values around the equator, lower ones south and north
446 of the equator. The most intense simulated CO enhancement around the equator fits the observed CO
447 enhancement of +125 ppb better when using GFED4 (90 ppb) than when using GFASv1.2 (75 ppb). However
448 the comparison also reveals an underestimation of the CO anomaly's amplitude by around 10 ppb to 25 ppb on
449 average by SOFT-IO. The model is thus only able to reproduce 75% to 90% of the peak concentrations on
450 average. Stroppiana et al. (2010) indeed showed that there are strong uncertainties in the fire emission
451 inventories over Africa (164 to 367 Tg CO per year).

452 **5 Statistical evaluation of the modeled CO enhancements in pollution plumes**

453 In this section, we present a statistical validation of the SOFT-IO calculations based on the entire IAGOS CO
454 data base (2003-2013). The ability of SOFT-IO in simulating CO anomalies is evaluated compared to in situ
455 measurements in terms of:

- 456 • spatial and temporal frequency of the plumes
- 457 • mixing ratio enhancements in the plumes

458 To achieve this, SOFT-IO performances are investigated over different periods of IAGOS measurements
459 depending on the emission inventory used. Three of the four global inventories selected previously (MACCity,
460 GFAS v1.2, GFED4) are available between 2003 and 2013. EDGAR v4.2 ends in 2008. In the following
461 sections (Sect.5.1 and 5.2), we discuss in detail the results obtained with MACCity and GFAS v1.2 between
462 2003 and 2013. Other emission inventory combinations are discussed in Sect. 5.3 when investigating SOFT-IO
463 sensitivity to input parameters.

464 **5.1 Detection frequency of the observed plumes with SOFT-IO**

465 The ability of SOFT-IO to reproduce CO enhancements was investigated using CO plumes obtained applying the
466 methodology described in Sect. 3.4 on all flights of the IAGOS database between 2003 and 2013. The frequency

467 of simulated plumes that coincide with the observed C^A anomalies is then calculated. Simulated plumes are
468 considered when matching in time and space the observed plumes, while modeled CO is on average higher than
469 5 ppb within the plume. Note that at this stage, we do not consider the intensity of the plumes.
470 The resulting detection rates are presented in Fig. 9 for eight of the eleven regions shown in Fig. 4. Statistics are
471 presented separately for three altitude levels (Lower Troposphere 0-2 km, Middle Troposphere 2-8 km and
472 Upper Troposphere > 8 km). Figure 9 shows that SOFT-IO performance in detecting plumes is very good and
473 not strongly altitude or region-dependent. In the three layers (LT, MT and UT), detection rates are higher than
474 95% and even close to 100% in the LT where CO anomalies are often related to short-range transport. Detection
475 frequency slightly decreases in the MT and the UT where CO modeling accuracy suffers from larger errors in
476 vertical and horizontal transport. On the contrary CO anomalies in the LT are most of the times related to short-
477 range transport of local pollution, which are well represented in SOFT-IO. For four regions we found worse
478 results: South America MT and UT, Africa MT and North Asia UT but with still high detection frequency (82%
479 to 85%). Note that only relatively few plumes (313 to 3761) were sampled by the IAGOS aircraft fleet in these
480 regions.

481

482 **5.2 Intensity of the simulated plumes**

483 The second objective of SOFT-IO is to accurately simulate the intensity of the observed CO anomalies. Fig. 10a
484 displays the bias between the means of the observed and modeled plumes for the regions sampled by IAGOS and
485 in the three vertical layers (LT, MT and UT), and the bias of the standard deviations in black. As explained
486 above this bias is calculated for the 2003-2013 period and using both anthropogenic emission from MACCity
487 and biomass burning emissions from GFAS v1.2 and the APT plume detection methodology described in Sect.
488 3.4.

489 The most documented regions presenting CO polluted plumes (Europe, North America, Africa, North Atlantic
490 UT, Central Asia MT and UT, South America, South Asia UT) present low biases (lower than ± 5 ppb, and up to
491 ± 10 ppb for Central Asia MT, South America UT) and low bias of the standard deviations (± 10 ppb to ± 50
492 ppb), which demonstrate a high skill of SOFT-IO.

493 Over several other regions with less frequent IAGOS flights, however, biases are higher, around ± 10 -15 ppb for
494 Africa UT and South Asia MT; around ± 25 -50 ppb for Central Asia LT, South Asia LT and North Asia UT.
495 Except for the last region, the highest biases are found in the Asian lower troposphere, suggesting
496 misrepresentation of local emissions. This is supported by the highest biases of the standard deviations (from \pm
497 60 ppb to ± 160 ppb for Asian regions). Indeed there is a rapid increase of emissions in this large area (Tanimoto
498 et al., 2009) associated with high discrepancies between different emission inventories (Wang et al., 2013; Stein
499 et al., 2014) and underestimated emissions (Zhang et al., 2015).

500 It is important to note that the biases remain of the same order (± 10 -15 ppb) when comparing the first (Q1),
501 second (Q2) and third (Q3) quartiles of the CO anomalies observed and modeled within most of the regions (Fig.
502 10b). This confirms the good capacity of the SOFT-IO software in reproducing the CO mixing ratios anomaly in
503 most of the observed pollution plumes.

504 Differences become much larger when considering outlier values of CO anomalies (lower and upper whiskers, \pm
505 2.7σ or 99.3%, Fig. 10b), which means for exceptional events of very low and very high CO enhancements

506 (accounting for 1.4% of the CO plumes), with biases from ± 10 ppb to ± 50 ppb for most of the regions. Higher
507 discrepancies are found in the lower and the upper troposphere in two specific regions (North Asia UT and South
508 Asia LT) for these extreme CO anomalies. North Asia UT discrepancies varies from -100 ppb to +200 ppb and
509 from -50 ppb to +100 ppb for South Asia LT. Note that North Asia UT and South Asia LT present respectively
510 extreme pollution events related to pyro-convection (Nédélec et al., 2005) for the first region, and to strong
511 anthropogenic surface emissions (Zhang et al., 2012) for the second one. It may suggest that the model fails to
512 correctly reproduce the transport for some specific but rare events of pyro-convection, or these emission
513 inventories are under estimated for such specific events.

514 When looking at the origin of the different CO anomalies (Fig. 10c), most of them are dominated by
515 anthropogenic emissions, which account for more than 70% of the contributions on average, except for South
516 America and Africa, which are strongly influenced by biomass burning (Sauvage et al. 2005, 2007c; Yamasoe et
517 al., 2014). Discussing origins of the CO anomalies in detail is out of the scope of this study, but gives here some
518 sense on the model performance. It is interesting to note that two of the three regions most influenced by
519 anthropogenic emissions, South Asia LT and Central Asia LT, with more than 90% of the enhanced CO coming
520 from anthropogenic emissions, are the highest biased regions compared to observations. This is not the case for
521 Europe LT for example, which also has a high anthropogenic influence. As stated before, anthropogenic
522 emissions in Asia are more uncertain than elsewhere (Stein et al., 2014).

523
524 In order to go a step further in the evaluation of SOFT-IO in reproducing CO anomalies mixing ratios, Fig. 11
525 displays the monthly mean time series of the observed (black line) and calculated (blue line) CO anomalies in
526 three vertical layers (LT, MT and UT), and the standard deviation of the observations (gray) and calculations
527 (light blue). This graph provides higher temporal resolution of the anomalies. CO polluted plumes are displayed
528 here using MACCity and GFAS v1.2 over the 2003-2013 periods and for the two regions with the largest
529 number of observed CO anomalies, Europe and North America.

530 It is worth noting the good ability of SOFT-IO in quantitatively reproducing the CO enhancements observed by
531 IAGOS. This is especially noticeable in the LT and UT, with similar CO mixing ratios observed and modeled
532 during the entire period and within the standard deviation of the measurements. Standard deviation of the
533 observations is higher in LT where there are fewer measurements than in the UT. However, the amplitude of the
534 seasonal cycle of CO maxima is highly underestimated (-100%) after January 2009 in the European LT, where
535 anthropogenic sources are predominant with more than 90% influence (Fig. 10c). This suggests
536 misrepresentation of anthropogenic emissions in Europe after the year 2009. Indeed Stein et al., (2014)
537 suggested the lower near-surface CO bias was found in Europe in relation with possible under
538 estimation of traffic emissions in the inventories.

539 In the middle troposphere (2-8 km), the CO plumes are systematically overestimated by SOFT-IO by
540 50% to 100% compared to the observations, with larger standard deviation and higher overestimation
541 over NAM. This might be related to different reasons:

- 542 • the chosen methodology of the CO plume enhancements detection for those altitudes
543 (described in Sect. 3.4), which may lead to a large number of plumes with small CO

544 enhancements, which are difficult to simulate. This could be due to the difficulty in defining a
545 realistic CO background in the middle troposphere.

546 • the source-receptor transport which may be more difficult to simulate between 2-8 km than in
547 the LT where receptors are close to sources; or than in the UT where most of the plumes are
548 related to convection detrainment better represented in the models than MT detrainment which
549 might be less intense.

550 • The frequency of the IAGOS observations which is lower in the LT and in the MT than in the
551 UT.

552 • Higher overestimation over NAM MT than Eur MT could be first related to lower frequency
553 of measurements in the NAM. Moreover overestimation is greater during summer when NAM
554 MT is closer to summer sources such as boreal fires, while Eur MT is related to CO air masses
555 more diluted with background air during transatlantic transport.

556 Correlation coefficients between simulated and observed plumes are highest in the LT (0.56 to 0.79) and lower
557 (0.30 to 0.46) in the MT and in the UT, suggesting some difficulties for the model in lifting up pollution from the
558 surface to the UT.

559 **5.3 Sensitivity of SOFT-IO to input parameters**

560 Different factors influence the ability of SOFT-IO to correctly reproduce CO pollution plumes. Among them,
561 transport parameterizations (related to convection, turbulence, etc) are not evaluated in this study as they are
562 inherent of the FLEXPART model. In this section, the model sensitivity to the chosen emission inventory is
563 evaluated. For this, a set of sensitivity studies is performed to investigate different configurations of the emission
564 inventories :

- 565 • type of inventory: MACCity, EDGAR for anthropogenic, GFED4, GFAS v1.2 or ICARTT for biomass
566 burning
- 567 • biomass burning injection heights: DENTENER, MIXED or APT approach (detailed in Sect. 3.3).

568
569 SOFT-IO performances are then investigated using Taylor diagrams (Taylor et al. 2001). The methodology
570 (choice of regions, vertical layers, sampling periods) is similar to the one used to analyze the ability of the model
571 to correctly reproduce the frequency and the intensity of the CO plumes with MACCity and GFAS (Sect.5.1 and
572 Sec5.2).

573 **5.3.1 Anthropogenic emission inventories**

574 Sensitivity of SOFT-IO to anthropogenic emissions is investigated between 2002 and 2008, using GFAS with
575 MACCity or EDGARv4.2. Fig. 12a presents a Taylor diagram for the two configurations (dots for MACCity,
576 crosses for EDGAR) for the regions and for the vertical layers described previously (Sect. 5.1 and Sect. 5.2),
577 while Fig. 12b represents the mean bias between each model configuration and the IAGOS observations.

578 As already seen in Sect. 4.1 for the case studies chosen to investigate anthropogenic emissions, slightly better
579 results seem to be obtained with MACCity. The Taylor diagram shows for most of the regions higher
580 correlations and lower biases in this case. These results are not surprising, as MACCity (Lamarque et al., 2010;

581 Grenier et al., 2011) is a more recent inventory compared to EDGARv4.2 (Janssens-Maenhout et al., 2010), and
582 expected to better represent anthropogenic emissions. However as stated in Lamarque et al., (2010) both
583 inventories share many aspects (for example over Latin and South America), and the differences between the
584 two inventories are most of the time very low, as global emission inventories tend to be quite similar.
585 Regionally, however, results with EDGARv4.2 can be better by almost 50%, such as over South Asia LT and
586 MT, Central Asia LT and MT. This supports our choice of maintaining several different inventories in SOFT-IO.

587 **5.3.2 Biomass burning emissions**

588 We first investigate the sensitivity of SOFT-IO to the type of biomass burning inventory, using MACCity with
589 GFAS v1.2 or GFED 4 (2003-2013), using the same MIXED methodology for vertical injection of emissions
590 (Fig. 2). As for anthropogenic emissions, Fig. 13 represents the Taylor diagram and averaged biases for the
591 different configurations.

592 Performances (correlations, standard deviations and biases) are very similar for both biomass burning
593 inventories, with smaller differences compared to anthropogenic inventories. Even for regions dominated by
594 biomass burning such as Africa or South America as depicted previously (Fig. 11c), the sensitivity of the SOFT-
595 IO performance to the type of global fire inventory is below 5 ppb.

596

597 Based on case studies, we discussed in Sect. 4.2 the comparison of CO contributions modeled using regional fire
598 emission inventories. It resulted in a better representation of biomass burning plumes using the specifically
599 designed campaign inventory than using the global inventories (Table 4). However, there is no clear evidence of
600 this result when investigating the model performances during the whole summer 2008. On contrary to Sect. 4.2,
601 it is hard to conclude of systematic better results using the ICARTT inventory. While simulations (not shown)
602 give better results for a few specific events of very high CO using ICARTT, similarly good results are obtained
603 when using GFASv1.2 or GFED4 for most other cases. It is worth noting that IAGOS samples biomass burning
604 plumes far from ICARTT sources, after dispersion and diffusion during transport in the atmosphere. Besides,
605 few boreal fire plumes (that would be better represented using ICARTT), are sampled by the IAGOS program.

606

607 Secondly, we investigate the influence of the vertical injection scheme for the biomass burning emissions, using
608 the three methodologies for determining injection heights described in Sect. 3.3. Sensitivity tests (Fig. 13c and
609 Fig 13d) demonstrate a small influence of the injection scheme on the simulated plumes. The largest influence is
610 found over North Asia UT, where pyro-convection has been highlighted in the IAGOS observations (Nédélec et
611 al., 2005), with however less than 5 ppb difference between the different schemes. More generally, small vertical
612 injection influence is probably due to too few cases where boreal fire emissions are injected outside the PBL by
613 pyro-convection, as shown in the Paugam et al. (2016) study, combined with a too low sampling frequency of
614 boreal fire plumes by IAGOS.

615

616 **6 Conclusions**

617

618 Analyzing long term in situ observations of trace gases can be difficult without a priori knowledge of the
619 processes driving their distribution and seasonal/regional variability, like transport and photochemistry. This is
620 particularly the case for the extensive IAGOS database, which provides a large number of aircraft-based in-situ
621 observations (more than 51000 flights so far) distributed on a global scale, and with no a priori sampling
622 strategy, unlike dedicated field campaigns.

623

624 In order to help studying and analyzing such a large data set of in situ observations, we developed a system that
625 allows quantifying the origin of trace gases both in terms of geographical location as well as source type. The
626 SOFT-IO module (<https://doi.org/10.25326/2>) is based on the FLEXPART particle dispersion model that is run
627 backward from each trace gas observation, and on different emission inventories (EDGAR v4.2, MACCity,
628 GFED 4, GFAS v1.2) than can be easily changed.

629

630 The main advantages of the SOFT-IO module are:

- 631 • Its flexibility. Source-receptor relationships pre-calculated with the FLEXPART particle dispersion
632 model can be coupled easily with different emission inventories, allowing each user to select model
633 results based on a range of different available emission inventories.
- 634 • CO calculation, which is computationally very efficient, can be repeated easily whenever updated
635 emission information becomes available without running again the FLEXPART model. It can also be
636 extended to a larger number of emission datasets, particularly when new inventories become available,
637 or for emission inventories inter-comparisons. It can also be extended to other species with similar or
638 longer lifetime as CO to study other type of pollution sources.
- 639 • High sensitivity of the SOFT-IO CO mixing ratios to source choice for very specific regions and case
640 studies, especially in the LT most of the time driven by local or regional emissions, may also help
641 improving emission inventories estimates through evaluation with a large database such as IAGOS one.
642 Indeed as it is based on a Lagrangian dispersion model, the tool presented here is able to reproduce
643 small-scale variations, which facilitates comparison to in situ observations. It can then be used to
644 validate emission inventories by confronting them to downwind observations of the atmospheric
645 composition, using large database of in situ observations of recent pollution.
- 646 • More generally SOFT-IO can be used in the future for any kind of atmospheric observations (e.g.
647 ground based measurements, satellite instruments, aircraft campaigns) of passive tracers.

648

649 In this study SOFT-IO is applied to all IAGOS CO observations, using ECMWF operational meteorological
650 analysis and 3-hour forecast fields and inventories of anthropogenic and biomass burning emissions available on
651 the ECCAD portal. SOFT-IO outputs are evaluated first at the examples of case studies of anthropogenic and
652 biomass burning pollution events. The evaluation is then extended statistically, for the entire 2003-2013 period,
653 over 14 regions and 3 vertical layers of the troposphere.

654

655 The main results are the following:

- 656 • By calculating the contributions of recent emissions to the CO mixing ratio along the flight tracks,
657 SOFT-IO identifies the source regions responsible for the observed pollution events, and is able to
658 attribute such plumes to anthropogenic and/or biomass burning emissions.
- 659 • On average, SOFT-IO detects 95% of all observed CO plumes. In certain regions, detection frequency
660 reaches almost 100%.
- 661 • SOFT-IO gives a good estimation of the CO mixing ratio enhancements for the majority of the regions
662 and the vertical layers. In majority, the CO contribution is reproduced with a mean bias lower than 10-
663 15 ppb, except for the measurements in the LT of Central and South Asia and in the UT of North Asia
664 where emission inventories seems to be less accurate.
- 665 • CO anomalies calculated by SOFT-IO are very close to observations in the LT and UT where most of
666 the IAGOS data are recorded. Agreement is lower in the MT, possibly because of numerous thinner
667 plumes of lower intensity (maybe linked to the methodology of the plume selection).
- 668 • SOFT-IO has less skill in modeling CO in extreme plume enhancements with biases higher than 50 ppb.
669

670 In its current version, SOFT-IO is limited by different parameters, such as inherent parameterization of the
671 Lagrangian model, but also by input of external parameters such as meteorological field analysis and emission
672 inventories. Sensitivity analyses were then performed using different meteorological analysis and emissions
673 inventories, and are summarized as follow:

- 674 • Model results were not very sensitive to the resolution of the meteorological input data. Increasing the
675 resolution from 1 deg to 0.5 deg resulted only in minor improvements. On the other hand, using
676 operational meteorological analysis allowed more accurate simulations than using ERA-Interim
677 reanalysis data, perhaps related to the better vertical resolution of the former.
- 678 • Concerning anthropogenic emissions sensitivity tests, results display regional differences depending on
679 the emission inventory choice. Slightly better results are obtained using MACCity.
- 680 • Model results were not sensitive to biomass burning global inventories, with good results using either
681 GFED 4 or GFAS v1.2. However, a regional emission inventory shows better results for few individual
682 cases with high CO enhancements. There is a low sensitivity to parameterizing the altitude of fire
683 emission injection, probably because events of fires injected outside of the PBL are rare or because
684 IAGOS does not frequently sample of such events

685

686 Using such CO calculations and partitioning makes it possible to link the trends in the atmospheric composition
687 with changes in the transport pathways and/or changes of the emissions.

688 SOFT-IO products will be made available through the IAGOS central database (<http://iagos.sedoo.fr/#L4Place>)
689 and are part of the ancillary products (<https://doi.org/10.25326/3>)

690
691

692 **Acknowledgements**

693

694 The authors would like to thanks ECCAD project for providing emission inventories. The authors acknowledge
695 the strong support of the European Commission, Airbus, and the Airlines (Lufthansa, Air-France, Austrian, Air
696 Namibia, Cathay Pacific, Iberia and China Airlines so far) who carry the MOZAIC or IAGOS equipment and
697 perform the maintenance since 1994. In its last 10 years of operation, MOZAIC has been funded by INSU-
698 CNRS (France), Météo-France, Université Paul Sabatier (Toulouse, France) and Research Center Jülich (FZJ,
699 Jülich, Germany). IAGOS has been additionally funded by the EU projects IAGOS-DS and IAGOS-ERI. The
700 MOZAIC-IAGOS database is supported by AERIS (CNES and INSU-CNRS). The former CNES-ETHER
701 program has funded this project.

702

703

704

705 **References**

706

707 Barret, B., Sauvage, B., Bennouna, Y., and Le Flochmoen, E.: Upper-tropospheric CO and O₃ budget during the
708 Asian summer monsoon, *Atmos. Chem. Phys.*, 16, 9129-9147, doi:10.5194/acp-16-9129-2016, 2016

709 Beirle, S; Spichtinger, N; Stohl, A; et al.: Estimating the NO(x) produced by lightning from GOME and NLDN
710 data: a case study in the Gulf of Mexico, *Atm. Chem. Phys.*, 6, 1075-1089, 2006.

711 Boden, T.A., G. Marland, and R.J. Andres. 2015. Global, Regional, and National Fossil-Fuel CO₂ Emissions.
712 Carbon Dioxide Information Analysis Center, Oak Ridge National Laboratory, U.S. Department of Energy, Oak
713 Ridge, Tenn., U.S.A. doi 10.3334/CDIAC/00001_V2015, 2015

714 Cammas, J.-P., Brioude, J., Chaboureau, J.-P., Duron, J., Mari, C., Mascart, P., N'ed'elec, P., Smit, H., Pätz,
715 H.W., Volz-Thomas, A., Stohl, A., and Fromm, M.: Injection in the lower stratosphere of biomass fire emissions
716 followed by long-range transport: a MOZAIC case study, *Atm. Chem. Phys.*, 9, 5829-5846, [http://www. atmos-
717 chem-phys.net/9/5829/2009/](http://www.atmos-chem-phys.net/9/5829/2009/), 2009.

718 Clark, Hannah, Bastien Sauvage, Valerie Thouret, Philippe Nedelec, Romain Blot, Kuo-Ying Wang, Herman
719 Smit, et al.: The First Regular Measurements of Ozone, Carbon Monoxide and Water Vapour in the Pacific
720 UTLS by IAGOS, *Tellus B*, 67. doi:10.3402/tellusb.v67.28385, 2015.

721 Cooper, O. R.; Stohl, A.; Trainer, M.; et al : Large upper tropospheric ozone enhancements above midlatitude
722 North America during summer: In situ evidence from the IONS and MOZAIC ozone measurement network, *J.*
723 *Geophys. Res.*, 111, D24, 2006.

724 Cristofanelli, P., Fierli, F., Marinoni, A., Calzolari, F., Duchi, R., Burkhart, J., Stohl, A., Maione, M., Arduini, J.,
725 and Bonasoni, P.: Influence of biomass burning and anthropogenic emissions on ozone, carbon monoxide and
726 black carbon at the Mt. Cimone GAW-WMO global station (Italy, 2165 m a.s.l.), *Atmos. Chem. Phys.*, 13, 15-
727 30, doi:10.5194/acp-13-15-2013, 2013

728 Damoah, R., Spichtinger, N., Forster, C., James, P., Mattis, I., Wandinger, U., Beirle, S., Wagner, T., and Stohl,
729 A.: Around the world in 17 days -hemispheric-scale transport of forest fire smoke from Russia in May 2003,
730 *Atm. Chem. Phys.*, 4, 1311-1321, 2004.

731 Dentener, F., Kinne, S., Bond, T., Boucher, O., Cofala, J., Generoso, S., Ginoux, P., Gong, S., Hoelzemann, J. J.,
732 Ito, A., Marelli, L., Penner, J. E., Putaud, J.-P., Textor, C., Schulz, M., van der Werf, G. R., and Wilson, J.:
733 Emissions of primary aerosol and precursor gases in the years 2000 and 1750 prescribed data-sets for AeroCom,
734 *Atmos. Chem. Phys.*, 6, 4321-4344, doi:10.5194/acp-6-4321-2006, 2006

735 Ding, A., T. Wang, and C. Fu (2013), Transport characteristics and origins of carbon monoxide and ozone in
736 Hong Kong, South China, *J. Geophys. Res. Atmos.*, 118, 9475-9488, doi:10.1002/jgrd.50714, 2013

737 Eastham, S. D. and Jacob, D. J.: Limits on the ability of global Eulerian models to resolve intercontinental
738 transport of chemical plumes, *Atmos. Chem. Phys.*, 17, 2543-2553, doi:10.5194/acp-17-2543-2017, 2017.

739 Elguindi, N., Clark, H., Ordonez, C., Thouret, V., Flemming, J., Stein, O., Huijnen, V., Moinat, P., Inness, A.,
740 Peuch, V.-H., Stohl, A., Turquety, S., Athier, G., Cammas, J.-P., and Schultz, M.: Current status of the ability of
741 the GEMS/MACC models to reproduce the tropospheric CO vertical distribution as measured by MOZAIC,
742 *Geosci. Model Dev.*, 3, 501-518, <http://www.geosci-model-dev.net/3/501/2010/>, 2010.

743 Freitas, S. R., Longo, K. M., Chatfield, R., Latham, D., Silva Dias, M. A. F., Andreae, M. O., Prins, E., Santos, J.
744 C., Gielow, R., and Carvalho Jr., J. A.: Including the sub-grid scale plume rise of vegetation fires in low

745 resolution atmospheric transport models, *Atmos. Chem. Phys.*, 7, 3385-3398, doi:10.5194/acp-7-3385-2007,
746 2007

747 Giglio, S., Randerson, J.T., Van der Werf, G.R.: Analysis of daily, monthly, and annual burned area using the
748 fourth-generation global fire emissions database (GFED4), *J. Geophys. Res.*, 10.1002/jgrg.20042, 2013

749 Good, P., Giannakopoulos, C., O'Connor, F.M., Arnold, S.R., de Reus, M., Schlager, H.: Constraining
750 tropospheric mixing timescales using airborne observations and numerical models, *Atm. Chem. Phys.*, 3, 1023-
751 1035, 2003.

752 Granier, C., Bessagnet, B., Bond, T., D'Angiola, A., Denier van der Gon, H., Frost, G., Heil, A., Kaiser, J.,
753 Kinne, S., Klimont, Z., Kloster, S., Lamarque, J.-F., Liousse, C., Masui, T., Meleux, F., Mieville, A., Ohara, T.,
754 Raut, J.-C., Riahi, K., Schultz, M., Smith, S., Thompson, A., van Aardenne, J., van der Werf, G., and van
755 Vuuren, D.: Evolution of anthropogenic and biomass burning emissions of air pollutants at global and regional
756 scales during the 1980-2010 period, *Climatic Change*, 109, 163–190, [http://dx.doi.org/10.1007/s10584-011-](http://dx.doi.org/10.1007/s10584-011-0154-1)
757 [0154-1](http://dx.doi.org/10.1007/s10584-011-0154-1), 10.1007/s10584-011-0154-1, 2011.

758 Granier, C., Damas, S., Liousse, C., Middleton, P., Mieville, A., et al. : The ECCAD Database: Emissions of
759 Atmospheric Compounds & Compilation of Ancillary Data. IGAC Newsletter, pp.18-20, 2012

760 Gressent, A., Sauvage, B., Defer, E. et al. : Lightning NO_x influence on large-scale NO_y and O₃ plumes
761 observed over the northern mid-latitudes, *Tellus B*, 66, 25544, 2014

762 Hanna, S. R.: Applications in air pollution modeling, *Atmospheric Turbulence and Air Pollution Modelling*,
763 1982.

764 Jacob, D.J.: *Introduction to Atmospheric Chemistry*, Princeton University Press, 1999

765 Janssens-Maenhout, G., Petrescu, A. M. R., Muntean, M., and Blujdea, V.: *Verifying Greenhouse Gas*
766 *Emissions: Methods to Support International Climate Agreements*, Greenhouse Gas Measurement and
767 Management, 2010.

768 Kaiser, J. W., Heil, A., Andreae, M. O., Benedetti, A., Chubarova, N., Jones, L., Morcrette, J. J., Razinger, M.,
769 Schultz, M. G., Suttie, M., and van der Werf, G. R.: Biomass burning emissions estimated with a global fire
770 assimilation system based on observed fire radiative power, *Biogeosciences*, 9, 527–554, 2012.

771 Liu, L., Logan, J.A., Murray, L.T., Pumphrey, H.C., Schwartz, M.J., Megretskaja, I.A.: Transport analysis and
772 source attribution of seasonal and interannual variability of CO in the tropical upper troposphere and lower
773 troposphere, *Atm. Chem. Phys.*, 13, 129-146, 2013.

774 Logan, J.A., Prather, M.J., Wofsy, S.C. et al. : *Tropospheric Chemistry – A Global Perspective*, *J. Geophys.*
775 *Res.*, 86, 7210-7254, 1981.

776 Marengo, A; Thouret, V; Nedelec, P; et al.: Measurement of ozone and water vapor by Airbus in-service aircraft:
777 The MOZAIC airborne program, An overview, *J. Geophys. Res.*, 103, D19, 1998.

778 Mauzerall, DL; Logan, JA; Jacob, DJ; et al. : Photochemistry in biomass burning plumes and implications for
779 tropospheric ozone over the tropical South Atlantic, *J. Geophys. Res.*, 103, D7, 1998.

780 Miyazaki, K., Eskes, H., Sudo, K., Boersma, K. F., Bowman, K., and Kanaya, Y.: Decadal changes in global
781 surface NO_x emissions from multi-constituent satellite data assimilation, *Atmos. Chem. Phys.*, 17, 807-837,
782 doi:10.5194/acp-17-807-2017, 2017

783 Nédélec, P., Thouret, V., Brioude, J., Sauvage, B., Cammas, J. P., and Stohl, A.: Extreme CO concentrations in
784 the upper troposphere over northeast Asia in June 2003 from the in situ MOZAIC aircraft data, *Geophys. Res.*
785 *Lett.*, 32, 2005.

786 Nedelec, P; Cammas, JP; Thouret, V; et al: An improved infrared carbon monoxide analyser for routine
787 measurements aboard commercial Airbus aircraft: technical validation and first scientific results of the MOZAIC
788 III programme, *Atm. Chem. Phys.*, 3, 1551-1564, 2003

789 Nedelec, P., Blot, R., Boulanger, D. et al.: Instrumentation on commercial aircraft for monitoring the
790 atmospheric composition on a global scale: the IAGOS system, technical overview of ozone and carbon
791 monoxide measurements, *Tellus B*, 67, 27791, 2015.

792 Newell, R.E., Thouret, V., Cho, J.Y.N., Stoller, P., Marenco, A., and Smit, H.G.S.: Ubiquity of quasi-horizontal
793 layers in the atmosphere, *Nature*, 398, 316-319, doi:10.1038/18642, 1999

794 Paugam, R., Wooster, M., Atherton, J., Freitas, S. R., Schultz, M. G., and Kaiser, J. W.: Development and
795 optimization of a wildfire plume rise model based on remote sensing data inputs – Part 2, *Atmos. Chem. Phys.*
796 *Discuss.*, 15, 9815-9895, doi:10.5194/acpd-15-9815-2015, 2015

797 Paugam, R., Wooster, M., Freitas, S. R., and Val Martin, M.: A review of approaches to estimate wildfire plume
798 injection height within large scale atmospheric chemical transport models, *Atmos. Chem. Phys.*, 16, 907-925,
799 doi:10.5194/acpd-16-907-2016, 2016

800 Petzold, A., Thouret, V., Gerbig, C. et al.: Global-scale atmosphere monitoring by in-service aircraft –current
801 achievements and future prospects of the European Research infrastructure IAGOS, *Tellus B*, 67, 28452, 2015

802 Pisso, I., Real, E., Law, K.S., Legras, B., Bousserez, N., Attié, J.L., Schlager, H.: Estimation of mixing in the
803 troposphere from Lagrangian trace gas reconstructions during long-range pollution plume transport , *J. of*
804 *Geophys. Res.* , 114, D19301, 2010.

805 Rémy, S., Veira, A., Paugam, R., Sofiev, M., Kaiser, J. W., Marenco, F., Burton, S. P., Benedetti, A., Engelen,
806 R. J., Ferrare, R., and Hair, J. W.: Two global climatologies of daily fire emission injection heights since 2003,
807 *Atmos. Chem. Phys. Discuss.*, doi:10.5194/acp-2015-1048, in review, 2016

808 Rodean, H. C.: *Stochastic Lagrangian Models of Turbulent Diffusion*, vol. 26, American Meteorological Society,
809 1996.

810 Sauvage, B., Thouret, V., Cammas, J.P., Gheusi, F., Athier, G., and Nédélec P.: Tropospheric ozone over
811 Equatorial Africa: regional aspects from the MOZAIC data, *Atmos. Chem. Phys.*, 5, 311-335, 2005

812 Sauvage, B., V. Thouret, A. M. Thompson, J. C. Witte, J.-P. Cammas, P. Nédélec, and G. Athier: Enhanced
813 view of the “tropical Atlantic ozone paradox” and “zonal wave one” from the in situ MOZAIC and SHADOZ
814 data, *J. Geophys. Res.*, 111, *D01301*, doi:10.1029/2005JD006241, 2006.

815 Sauvage, B.; Thouret, V.; Cammas, J. -P.; et al.: Meridional ozone gradients in the African upper troposphere,
816 *Geophys. Res. Lett.*, 34, L03817, 2007a

817 Sauvage, B., R. V. Martin, A. van Donkelaar, and J. R. Ziemke: Quantification of the factors controlling tropical
818 tropospheric ozone and the South Atlantic maximum, *J. Geophys. Res.*, 112, D11309,
819 doi:10.1029/2006JD008008, 2007b

820 Sauvage B., Martin R.V., van Donkelaar A., Liu X., Chance K., Jaeglé L., Palmer P.I., Wu S. , Fu T.-M. :
821 Remote sensed and in situ constraints on processes affecting tropical ozone, *Atmospheric Chemistry and*
822 *Physics*, 7, 815-838, 2007c.

823 Seibert, P. and Frank, A.: Source-receptor matrix calculation with a Lagrangian particle dispersion model in
824 backward mode, *Atm. Chem. Phys.*, 4, 51–63, 2004

825 Staudt, A. C., Jacob, D. J., Logan, J. A., Bachiochi, D., Krishnamurti, T. N., and Sachse, G. W.: Continental
826 sources, transoceanic transport, and interhemispheric exchange of carbon monoxide over the Pacific, *J. Geophys.*
827 *Res.*, 106(D23), 32571–32590, 2001

828 Stein, O., Schultz, M.G., Bouarar, I., Clark, H., Huijnen, V., Gaudel, A., George, M., Clerbaux, C.: On the
829 wintertime low bias of Northern Hemisphere carbon monoxide found in global model simulations, *Atmos.*
830 *Chem. Phys.*, 14, 9295-9316, doi:10.5194/acp-14-9295-2014, 2014

831 Stohl, A., M. Hittenberger, and G. Wotawa: Validation of the Lagrangian particle dispersion model FLEXPART
832 against large scale tracer experiments, *Atmos. Environ.*, 32, 4245-4264, 1998

833 Stohl, A. and Thomson, D. J.: A density correction for Lagrangian particle dispersion models, *Boundary Layer*
834 *Meteorol.*, 90, 155–167, 1999.

835 Stohl, A., Eckhardt, S., Forster, C., James, P., and Spichtinger, N.: On the pathways and timescales of
836 intercontinental air pollution transport, *J. Geophys. Res.*, 107, 2002.

837 Stohl, A., Forster, C., Eckhardt, S., Spichtinger, N., Huntrieser, H., Heland, J., Schlager, H., Wilhelm, S.,
838 Arnold, F., and Cooper, O.: A backward modeling study of intercontinental pollution transport using aircraft
839 measurements, *J. Geophys. Res.*, 108, 2003.

840 Stohl, A., Forster, C., Frank, A., Seibert, P., and Wotawa, G.: Technical note: The Lagrangian particle dispersion
841 model FLEXPART version 6.2, *Atmos. Chem. Phys.*, 5, 2461-2474, doi:10.5194/acp-5-2461-2005, 2005

842 Stohl, A., Aamaas, B., Amann, M., Baker, L. H., Bellouin, N., Berntsen, T. K., Boucher, O., Cherian, R.,
843 Collins, W., Daskalakis, N., Dusinska, M., Eckhardt, S., Fuglestedt, J. S., Harju, M., Heyes, C., Hodnebrog, Ø.,
844 Hao, J., Im, U., Kanakidou, M., Klimont, Z., Kupiainen, K., Law, K. S., Lund, M. T., Maas, R., MacIntosh, C.
845 R., Myhre, G., Myriokefalitakis, S., Olivie, D., Quaas, J., Quennehen, B., Raut, J.-C., Rumbold, S. T., Samset, B.
846 H., Schulz, M., Seland, Ø., Shine, K. P., Skeie, R. B., Wang, S., Yttri, K. E., and Zhu, T.: Evaluating the climate
847 and air quality impacts of short-lived pollutants, *Atmos. Chem. Phys.*, 15, 10529-10566, doi:10.5194/acp-15-
848 10529-2015, 2015

849 Stroppiana, D., Brivio, P. A., Grégoire, J.-M., Liousse, C., Guillaume, B., Granier, C., Mieville, A., Chin, M.,
850 and Pétron, G.: Comparison of global inventories of CO emissions from biomass burning derived from remotely
851 sensed data, *Atm. Chem. Phys.*, 10, 12173–12189, <http://www.atmos-chem-phys.net/10/12173/2010/>, 2010.

852 Tanimoto, H., Ohara, T., Uno, I.: Asian anthropogenic emissions and decadal trends in springtime tropospheric
853 ozone over Japan: 1998-2007, *Geophys. Res. Letters*, doi: 10.1029/2009GL041382, 2009

854 Taylor, K. E., Summarizing multiple aspects of model performance in a single diagram, *Journal of Geophysical*
855 *Research*, 106, D7, 7183-7192, 2001

856 Tressol, M., Ordonez, C., Zbinden, R., Brioude, J., Thouret, V., Mari, C., Nedelec, P., Cammas, J.-P., Smit, H.,
857 Patz, H.-W., and Volz-Thomas, A.: Air pollution during the 2003 European heat wave as seen by MOZAIC
858 airliners, *Atm. Chem. Phys.*, 8, 2133–2150, 2008.

859 Turquety, S., Logan, J. A., Jacob, D. J., Hudman, R. C., Leung, F. Y., Heald, C. L., Yantosca, R. M., Wu, S.,
860 Emmons, L. K., Edwards, D. P., and Sachse, G. W.: Inventory of boreal fire emissions for North America in
861 2004: Importance of peat burning and pyroconvective injection, *J. Geophys. Res.*, 112, 2007.

862 Van der Werf, G. R., Randerson, J. T., Giglio, L., Collatz, G. J., Mu, M., Kasibhatla, P. S., Morton, D. C.,
863 DeFries, R. S., Jin, Y., and van Leeuwen, T. T.: Global fire emissions and the contribution of deforestation,
864 savanna, forest, agricultural, and peat fires (1997-2009), *Atm. Chem. Phys.*, 10, 11 707–11 735, 2010.

865 Tanimoto, H., Ohara, T., Uno, I.: Asian anthropogenic emissions and decadal trends in springtime tropospheric
866 ozone over Japan: 1998-2007, *Geophys. Res. Letters*, 36, L23802, doi:10.1029/2009GL041382, 2009

867 Thouret, V., Cho, J.Y.N., Newell, R.E., Larenco, A. and Smit, H.G.J.: General characteristics of tropospheric
868 trace constituent layers observed in the MOZAIC program, *J. of Geophys. Res.*, 105, D13, 17379-17392, doi:
869 10.1029/2000JD900238, 2000

870 Thouret, V., Cammas, J.-P., Sauvage, B., Athier, G., Zbinden, R., Nédélec, P., Simon, P., and Karcher, F.:
871 Tropopause referenced ozone climatology and inter-annual variability (1994–2003) from the MOZAIC
872 programme, *Atmos. Chem. Phys.*, 6, 1033-1051, doi:10.5194/acp-6-1033-2006, 2006

873 Vay, S. A., , Y. Choi, K. P. Vadrevu, D. R. Blake, S. C. Tyler, A. Wisthaler, A. Hecobian, Y. Kondo, G. S.
874 Diskin, G. W. Sachse, J-H. Woo, A. J. Weinheimer, J. F. Burkhart, A. Stohl, and P. O. Wennberg : Patterns of
875 CO₂ and radiocarbon across high northern latitudes during International Polar Year 2008. *J. Geophys. Res.* 116,
876 D14301, doi:10.1029/2011JD015643, 2011

877 Wang, X., Wang, Y., Hao, J., Kondo, Y., Irwin, M., Munger, J.W., Zhao, Y.: Top-down estimate of China's
878 black carbon emissions using surface observations: sensitivity to observation representativeness and transport
879 model error, *J. of Geophys. Res.*, 118, 5781-5795, doi: 10.1002/jgrd.50397, 2013.

880 Wen, D., Lin, J.C., Millet, D.B., et al.: A backward-time stochastic Lagrangian air quality model, *Atmos. Env.*
881 54, 373-386, 2012

882 Yamasoe, M.A.; Sauvage, B.; Thouret, V.; et al. : Analysis of tropospheric ozone and carbon monoxide profiles
883 over South America based on MOZAIC/IAGOS database and model simulations, *Tellus B*, 67, 27884, 2015

884 Yashiro, H., Sugawara, S., Sudo, K., Aoki, S., and Nakazawa, T.: Temporal and spatial variations of carbon
885 monoxide over the western part of the Pacific Ocean, *J. Geophys. Res.*, 114, D08305, doi:10.1029/2008jd010876,
886 2009

887 Zhang, Yiqiang; Liu, Hongyu; Crawford, James H.; et al. : Distribution, variability and sources of tropospheric
888 ozone over south China in spring: Intensive ozonesonde measurements at five locations and modeling analysis, *J.*
889 *of Geophys. Res.*, 117, D12304, 2012

890 Zhang, L., Henze, D.K., Grell, G.A. et al.: Constraining black carbon aerosol over Asia using OMI aerosol
891 absorption optical depth and the adjoint of GEOS-Chem, *Atmos. Chem. Phys.*, 15, 10281-10308,
892 doi:10.5194/acp-15-10281-2015, 2015

893
894
895
896
897
898
899
900
901

902
903
904

Date	Take-off	Landing	Used for choosing
10 March 2002	Frankfurt	Denver	Anthropogenic emission inventories
27 November 2002	Dallas	Frankfurt	Anthropogenic emission inventories
4 June 2003	Tokyo	Vienna	Fire injection heights (pyro-convection)
6 August 2003	Boston	Frankfurt	Fire injection heights
9 August 2003	Dubai	Frankfurt	Fire injection heights
10 August 2003	Frankfurt	Dallas	Fire injection heights
29 June 2004	Caracas	Frankfurt	Fire injection heights (pyro-convection)
30 June 2004	Frankfurt	Washington	Fire injection heights (pyro-convection) Fire inventories
22 July 2004	Frankfurt	Atlanta	Fire injection heights (pyro-convection) Fire inventories
22 July 2004	Douala	Paris	Fire injection heights (pyro-convection) Fire inventories
23 July 2004	Frankfurt	Atlanta	Fire injection heights (pyro-convection) Fire inventories
19 July 2005	München	Hong Kong	Anthropogenic emission inventories
22 October 2005	München	Hong Kong	Anthropogenic emission inventories
30 July 2008	Windhoek	Frankfurt	Fire injection heights Fire emission inventories
31 July 2008	Frankfurt	Windhoek	Fire injection heights Fire emission inventories

905 **Table 1: Case studies used to define model settings. Cases studies discussed in the manuscript are in bold**

906
907
908
909
910
911
912
913
914
915
916
917
918
919
920

Inventory	Temporal coverage	Horizontal resolution	Temporal resolution	Reference
<i>Anthropogenic emissions</i>				
MACCity	1960 – 2014 +	0.5° x 0.5°	Monthly	<i>Lamarque et al., 2010; Granier et al. (2011)</i>
EDGAR v4.2	1970 - 2008	0.5° x 0.5°	Yearly	<i>Janssens-Maenhout et al. (2010)</i>
<i>Biomass Burning emissions</i>				
GFED 4	1997 – 2017+	0.5° x 0.5°	Daily	<i>Giglio et al. (2013)</i>
GFAS v1.0	2002	0.5° x 0.5°	Daily	
GFAS v1.2	2003 – 2017 +	0.1° x 0.1°	Daily	<i>Kaiser et al. (2012)</i>
ICARTT	2004	1° x 1°	Daily	<i>Turquety et al. (2007)</i>

Table 2: List of emission inventories used in this study.

921
922
923
924
925
926
927
928
929
930
931
932
933
934
935
936
937
938
939
940
941
942
943
944
945
946
947
948
949
950
951
952
953
954
955
956
957

Flight	IAGOS anomaly	IAGOS std	MACCity anomaly	MACCity std	EDGAR anomaly	EDGAR std	Anomaly altitude
10 March 2002 Frankfurt – Denver	16.8	8.7	20.2	6.9	12.8	5.1	UT
27 November 2002 Dallas – Frankfurt	28.0	8.6	20.0	8.0	16.4	7.4	UT
19 July 2005 München - Hong Kong	130.1	97.8	45.8	9.7	34.6	7.7	PBL
22 October 2005 München - Hong Kong	157.9	105.1	170.7	109.8	103.9	62.0	PBL

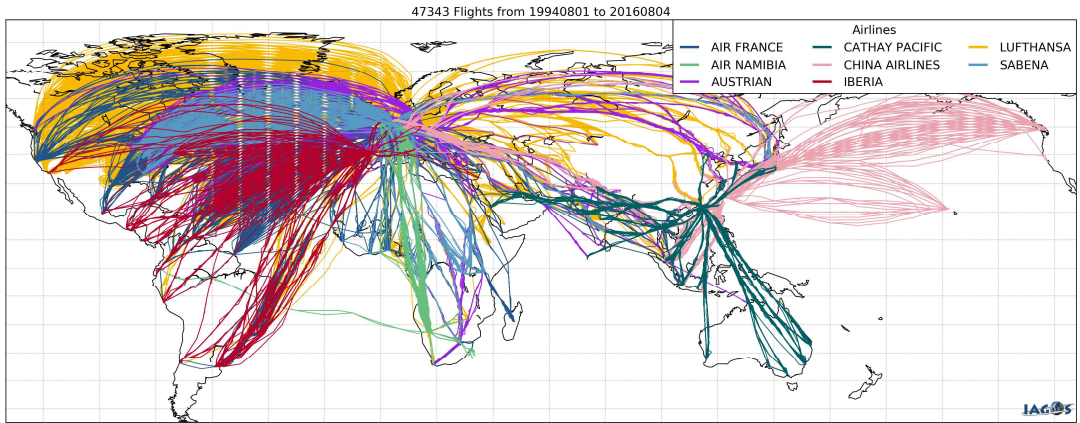
958 **Table 3. Summary of the averaged observed and simulated anomaly and corresponding averaged standard deviation**
959 **(std) (in ppb) determined for representing anthropogenic emissions for different case studies (using GFAS v1.2 for**
960 **biomass burning emissions). Altitude of the anomaly is indicated: boundary layer (PBL); middle troposphere (MT);**
961 **upper troposphere (UT)**

962
963
964
965
966
967
968
969
970
971
972
973
974
975
976
977
978
979
980
981
982
983
984
985
986
987
988

Flight	IAGOS anomaly	IAGOS std	GFAS v1.2 anomaly	GFAS v1.2 std	GFED4 anomaly	GFED4 std	ICARTT anomaly	ICARTT std	Anomaly altitude
29 June 2004 Caracas - Frankfurt	32.6	33.2	44.4	2.4	43.0	2.3	43.6	2.4	PBL
30 June 2004 Frankfurt - Washington	52.5	34.0	36.6	9.1	25.4	6.6	23.5	5.9	MT
22 July 2004 Frankfurt - Atlanta	87.0	35.0	42.8	17.6	45.8	18.9	39.7	15.7	MT
22 July 2004 Douala - Paris	117.1	24.2	43.5	20.0	55.0	27.2	72.4	42.3	MT
23 July 2004 Frankfurt - Atlanta	78.9	45.4	34.7	22.4	45.3	32.8	46.0	35.9	MT
30 July 2008 Windhoek - Frankfurt	72.9	41.9	33.0	19.2	42.8	26.0	N/A	N/A	UT
31 July 2008 Frankfurt - Windhoek	38.3	32.0	28.1	10.8	34.0	12.8	N/A	N/A	UT

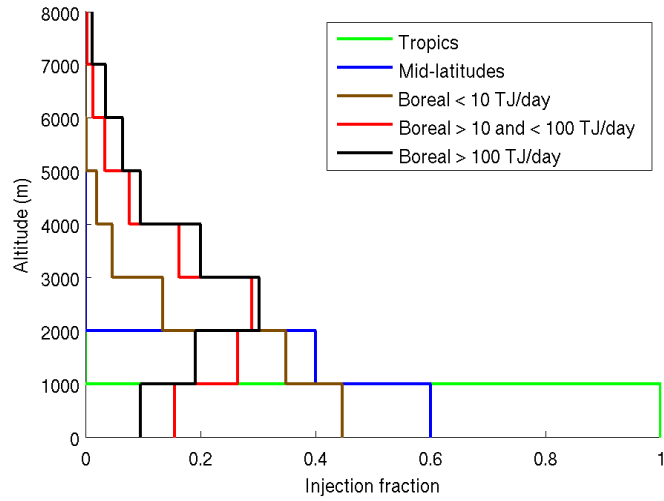
989 **Table 4. Summary of the averaged observed and simulated anomaly and corresponding averaged standard deviation**
990 **(std) (in ppb) determined for representing biomass burning emissions for different case studies (using MACCity for**
991 **anthropogenic emissions). Altitude of the anomaly is indicated: boundary layer (PBL); middle troposphere (MT);**
992 **upper troposphere (UT). Note that the ICARTT inventory is only available for summer 2004.**

993
994
995
996
997
998
999
1000
1001
1002
1003
1004
1005
1006
1007
1008
1009



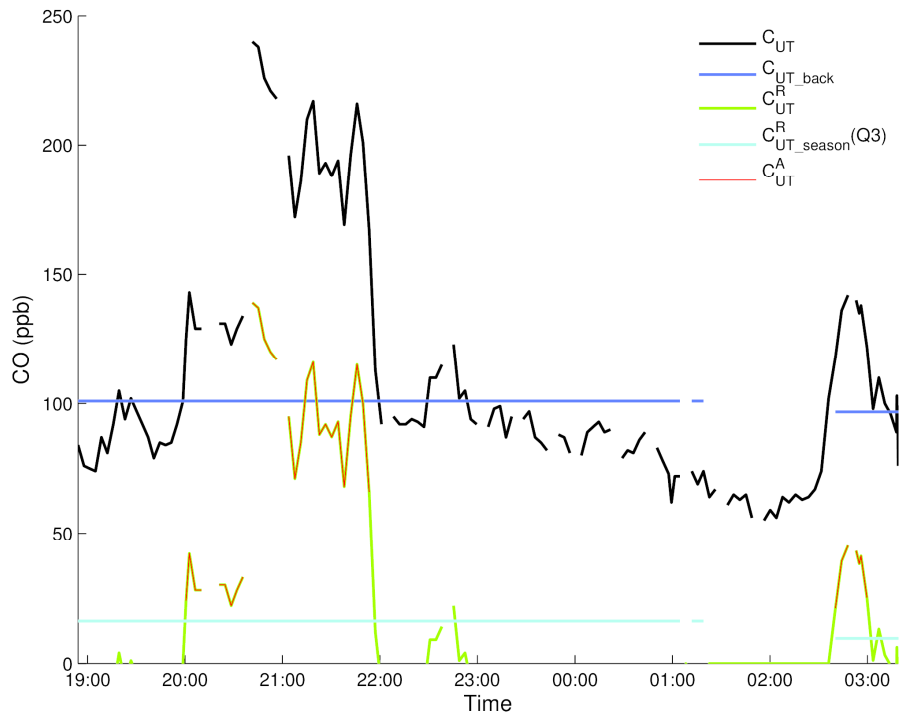
1010
1011 **Figure 1 : Map showing all flights performed by the IAGOS program**

- 1012
- 1013
- 1014
- 1015
- 1016
- 1017
- 1018
- 1019
- 1020
- 1021
- 1022
- 1023
- 1024
- 1025
- 1026
- 1027
- 1028
- 1029
- 1030
- 1031
- 1032
- 1033
- 1034
- 1035



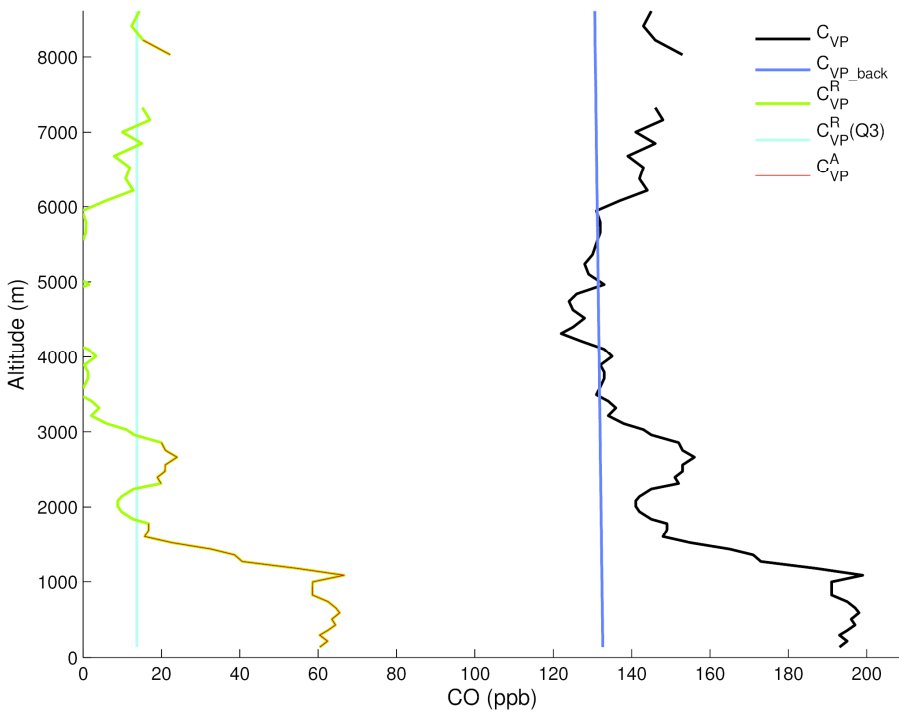
1036 **Figure 2: Injection profiles used for biomass burning emissions for different regions (Tropics, Mid-latitudes, Boreal)**
 1037 **in the MIXED methodology.**
 1038

1039
 1040
 1041
 1042
 1043
 1044
 1045
 1046
 1047
 1048
 1049
 1050



1051

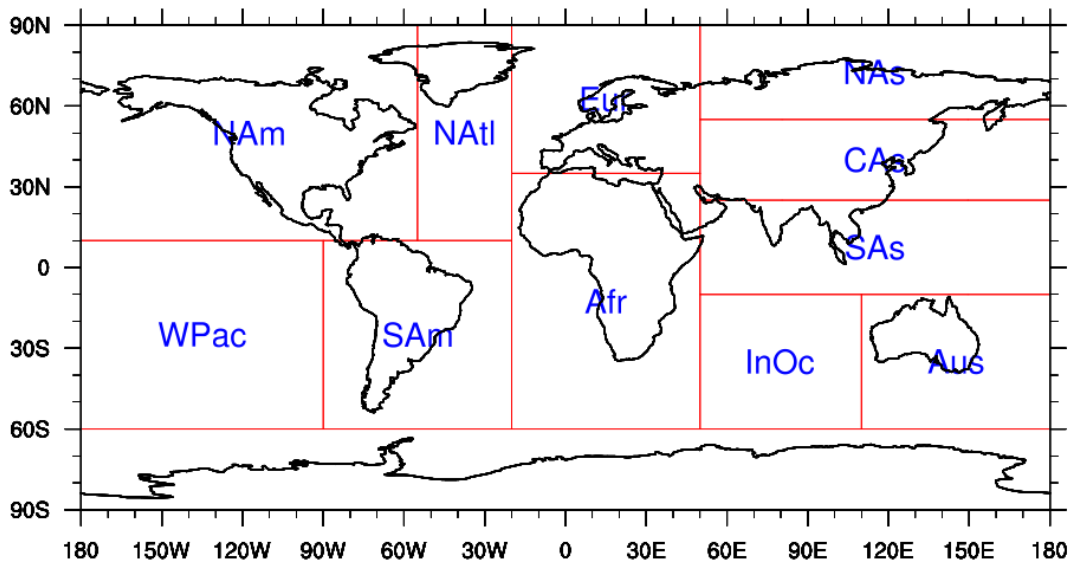
a)



1052

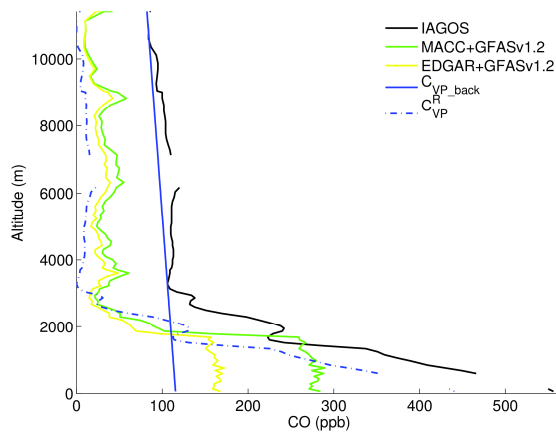
b)

1053 **Figure 3: Methodology used to extract CO anomalies along the flight track for (a) the cruise part of the flight and**
 1054 **(b) during take off and landing. Further details are given in section 3.4.**
 1055

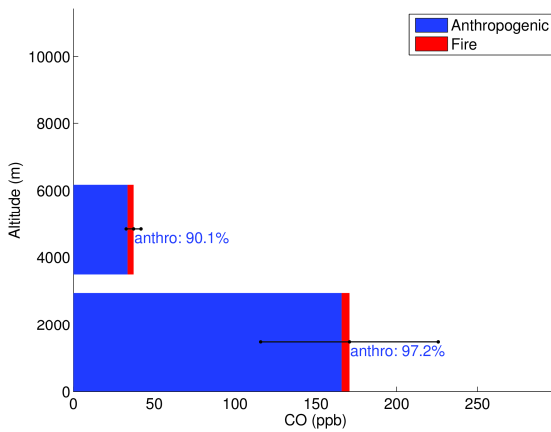


1056
 1057
 1058
 1059
 1060
 1061
 1062
 1063
 1064
 1065
 1066

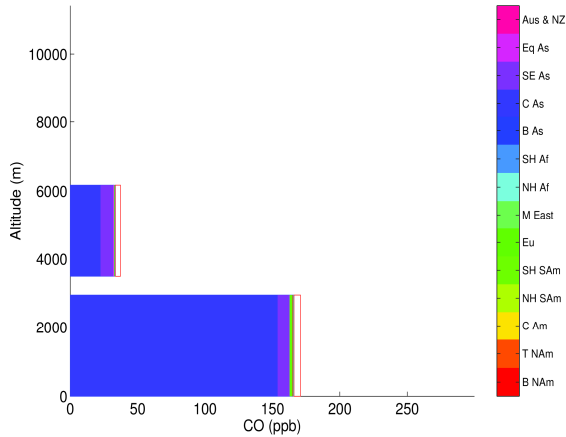
Figure 4: Map of the defined regions used to sort IAGOS CO anomalies



1067 a)



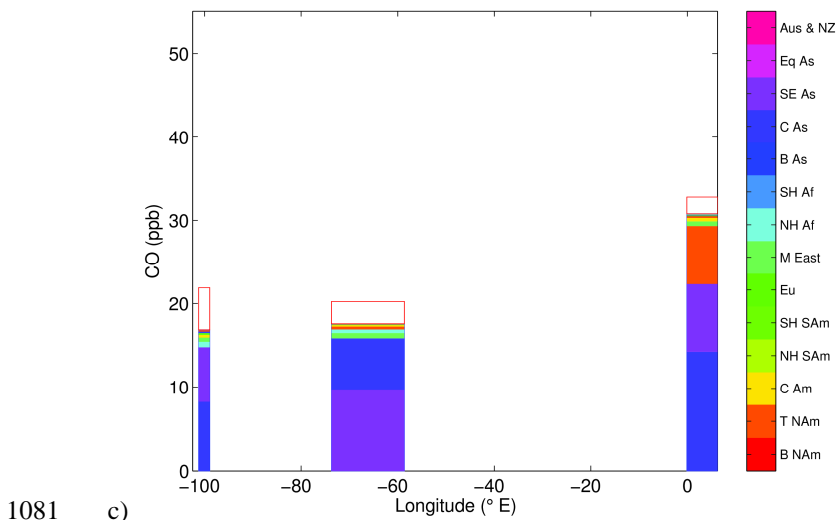
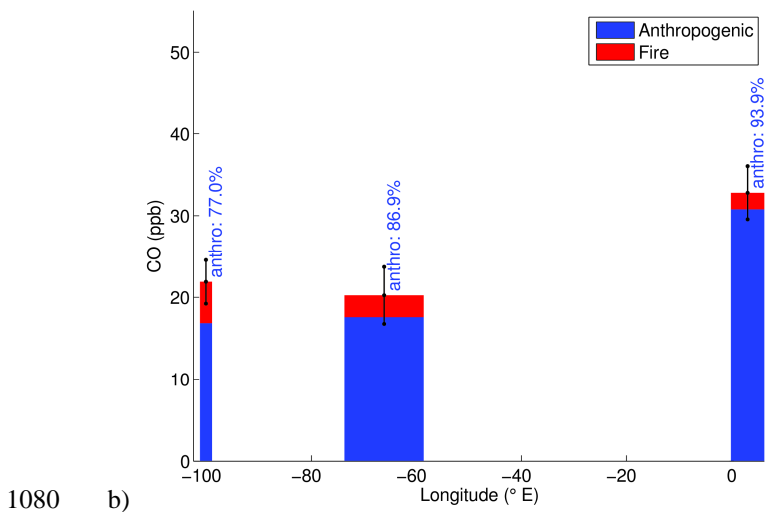
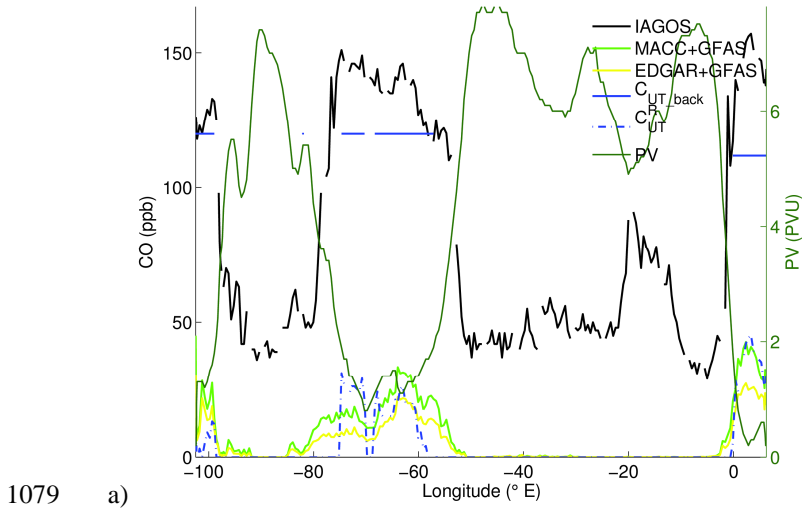
1068 b)



1069 c)

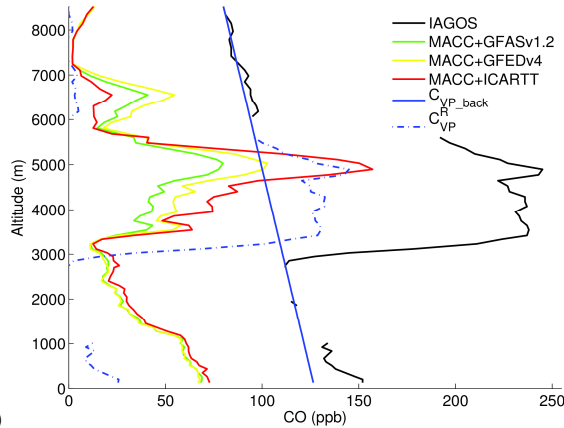
1070 **Figure 5: (a) Carbon monoxide profiles over Hong Kong during a MOZAIC-IAGOS flight landing on 22 October**
 1071 **2005. The black line indicates the observed CO profile while the blue line indicates the CO background deduced from**
 1072 **the observations. Green and yellow lines indicate the simulated CO contributions using respectively MACCcity and**
 1073 **EDGARv4.2 for anthropogenic emissions, and using GFAS v1.2 for biomass burning emissions. Simulated CO is**
 1074 **separated in (b) sources contribution (anthropogenic in blue, fires in red, standard deviation in black) and in (c)**
 1075 **regional anthropogenic origins (14 regions defined for global emission inventory,**
 1076 **<http://www.globalfiredata.org/data.html>, see Fig. S1; unshaded red square is for fire contribution), using MACCcity**
 1077 **and GFASv1.2.**

1078

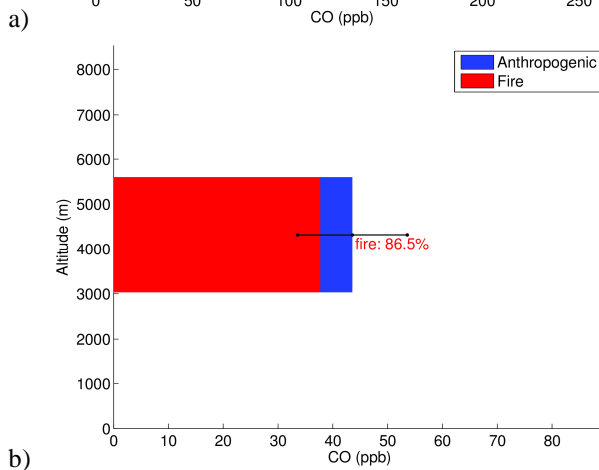


1082 **Figure 6: (a) Carbon monoxide zonal profile during the 10 March 2002 MOZAIC-IAGOS flight from Frankfurt to**
 1083 **Denver. The black line indicates the observed CO while the blue line indicates CO seasonal background in the UT**
 1084 **deduced from the IAGOS data set. Light green and yellow lines indicate the simulated contributions using**
 1085 **respectively MACCcity and EDGARv4.2 for anthropogenic emissions, and GFAS v1.0 for biomass burning emissions.**
 1086 **Dark green represents potential vorticity (pvu) from ECMWF analyses. Simulated CO is separated in (b) sources**
 1087 **contribution (anthropogenic in blue, fires in red, standard deviation in black) and in (c) regional anthropogenic**
 1088 **origins (14 regions defined for global emission inventory, <http://www.globalfiredata.org/data.html>, see Fig. S1;**
 1089 **unshaded red square is for fire contribution), using MACCcity and GFASv1.0.**

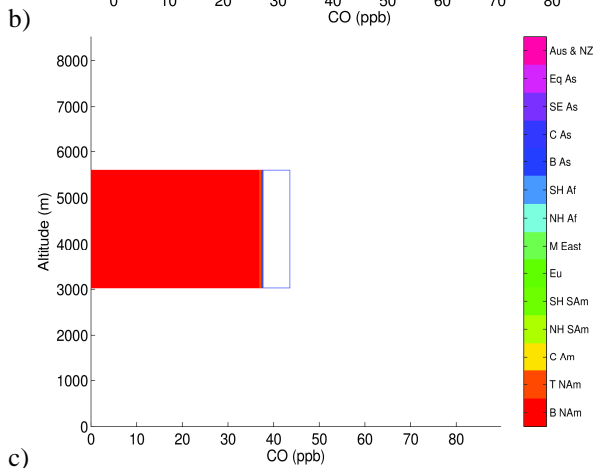
1090
 1091
 1092
 1093
 1094
 1095



1096



1097



1098

1099

1100

1101

1102

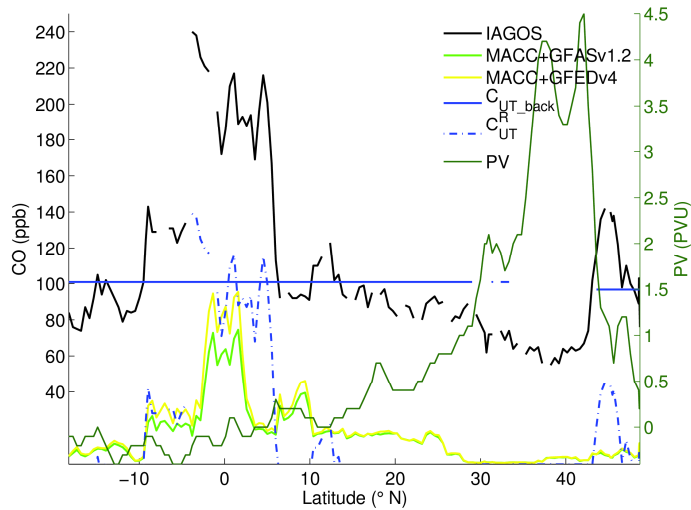
1103

1104

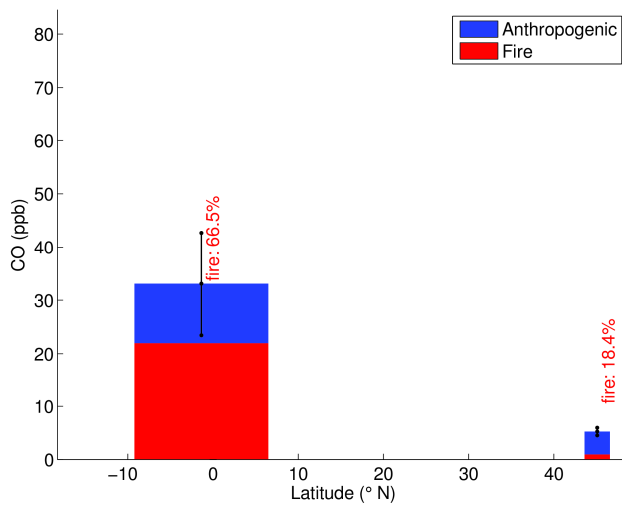
1105

Figure 7 : (a) Carbon monoxide profiles over Paris during a MOZAIC-IAGOS flight landing on 22 July 2004. The black line indicates the observed CO profile and the blue line indicates CO background deduced from the observations. Green, yellow and red lines indicate the simulated contributions using respectively GFASv1.2, GFED4 and ICARTT for biomass burning emissions, with MACCity for anthropogenic emissions. Simulated CO is separated in (b) sources contribution (anthropogenic in blue, fires in red, standard deviation in black) and in (c) regional biomass burning origins (14 regions defined for global emission inventory, <http://www.globalfiredata.org/data.html> see Fig. S1; unshaded blue square is for anthropogenic contribution), using MACCity and GFASv1.2.

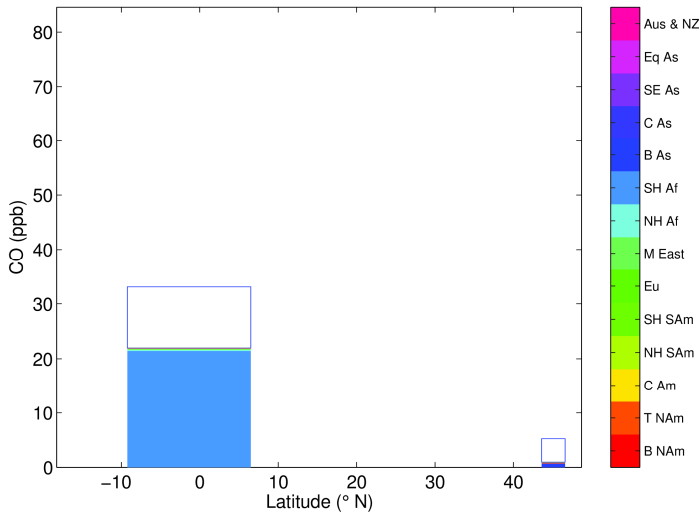
1106



1107 a)



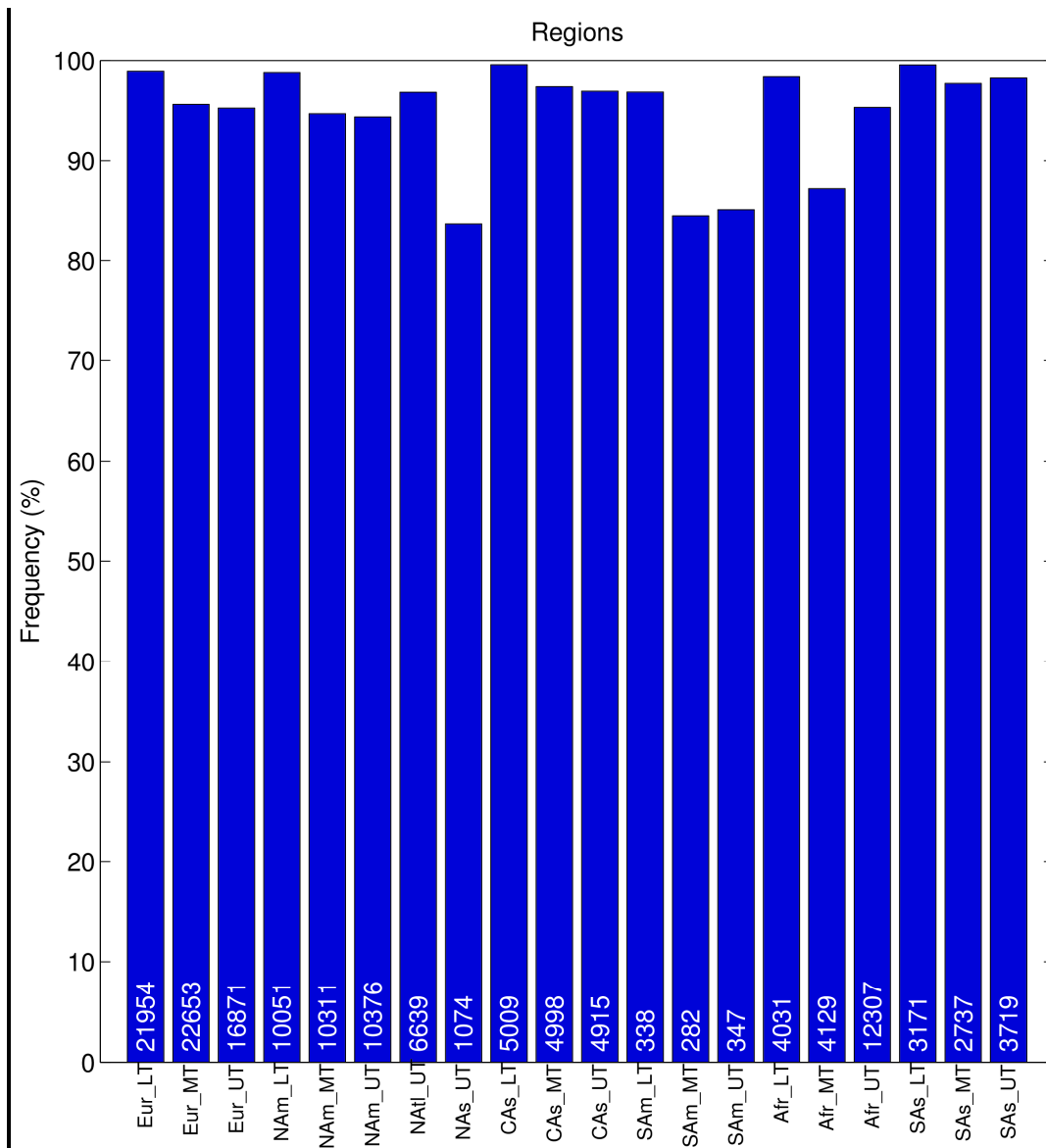
1108 b)



1109 c)

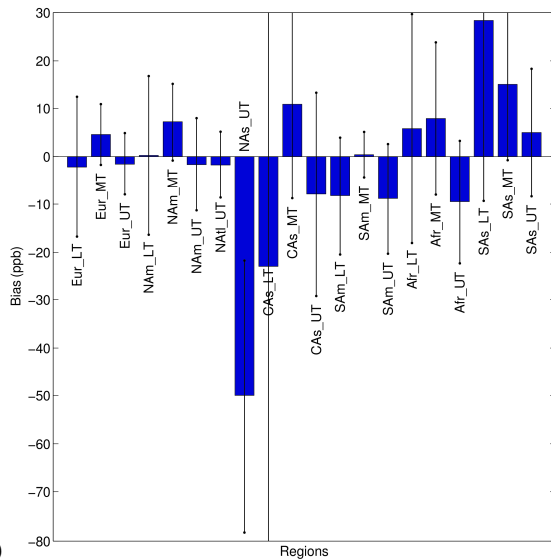
1110 **Figure 8:** (a) Carbon monoxide as a function of latitude during the 30 July 2008 MOZAIC-IAGOS flight from
 1111 Windhoek to Frankfurt. The black line indicates the observed CO, the blue line indicates the CO seasonal
 1112 background deduced from the IAGOS data set and the dash-dotted line the residual CO mixing ratio. Light green and
 1113 yellow lines indicate the simulated contributions using MACCcity for anthropogenic emissions, and respectively GFAS
 1114 v1.2 and GFED4 for biomass burning emissions. Dark green represents potential vorticity (pvu) from ECMWF
 1115 analyses. Simulated CO is separated in (b) sources contribution (anthropogenic in blue, fires in red, standard
 1116 deviation in black) and in (c) regional biomass burning origins (14 regions defined for global emission inventory,
 1117 <http://www.globalfiredata.org/data.html>, see Fig. S1; unshaded blue square is for anthropogenic contribution), using
 1118 MACCcity and GFASv1.2.

1119

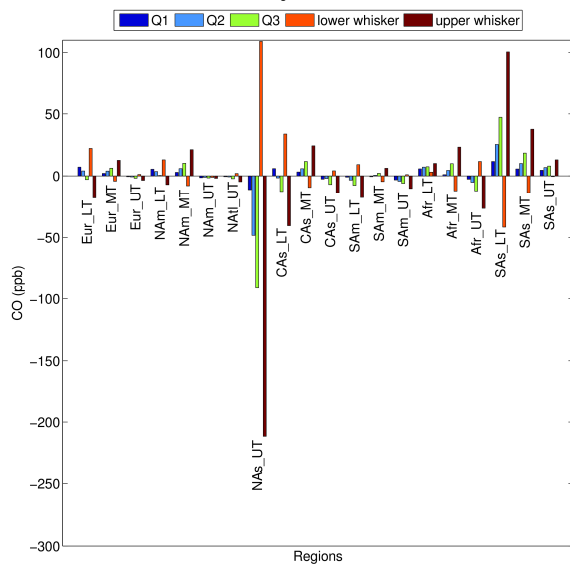


1120
 1121
 1122
 1123
 1124
 1125
 1126
 1127
 1128
 1129
 1130
 1131
 1132
 1133
 1134
 1135
 1136

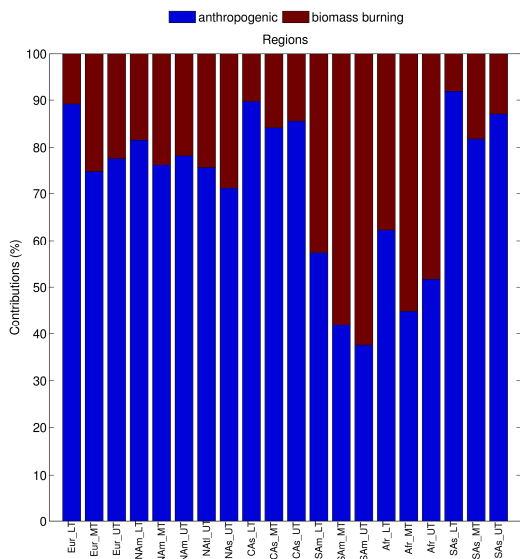
Figure 9: Frequency of plume detection (a) in different regions / altitudes / seasons using the MACCity and GFAS v1.2 emission inventories during the 2003-2013 period. Biomass burning vertical injection uses APT methodology. Altitude levels stand for LT=0-2km, MT=2-8km and UT=8km-tropopause. The numbers of the plumes observed in each case are displayed in each box.



1137 a)



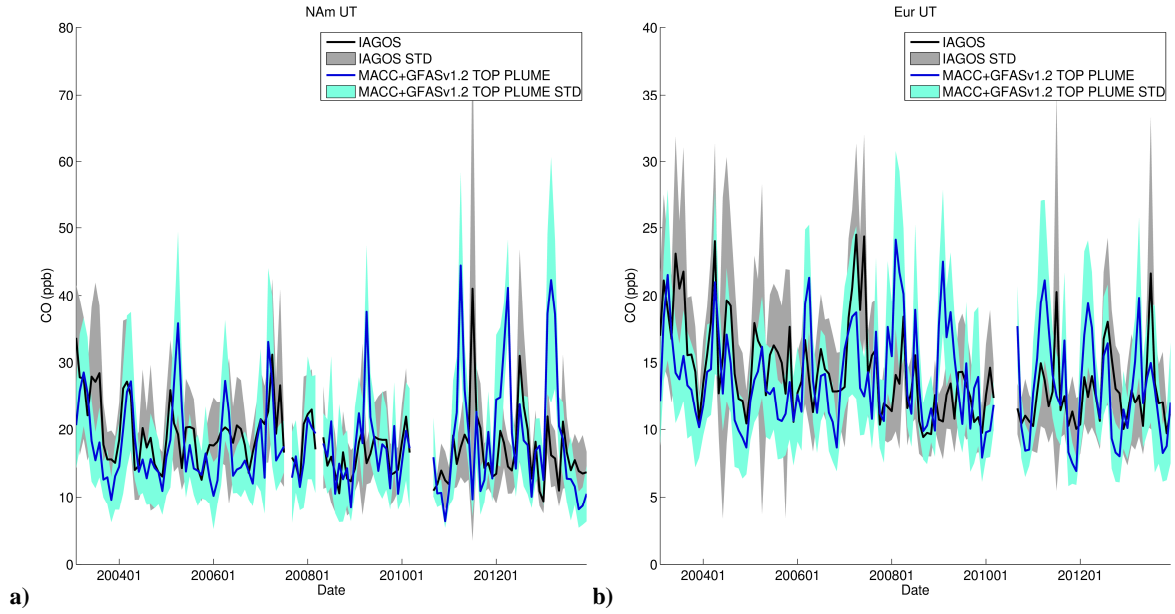
1138 b)



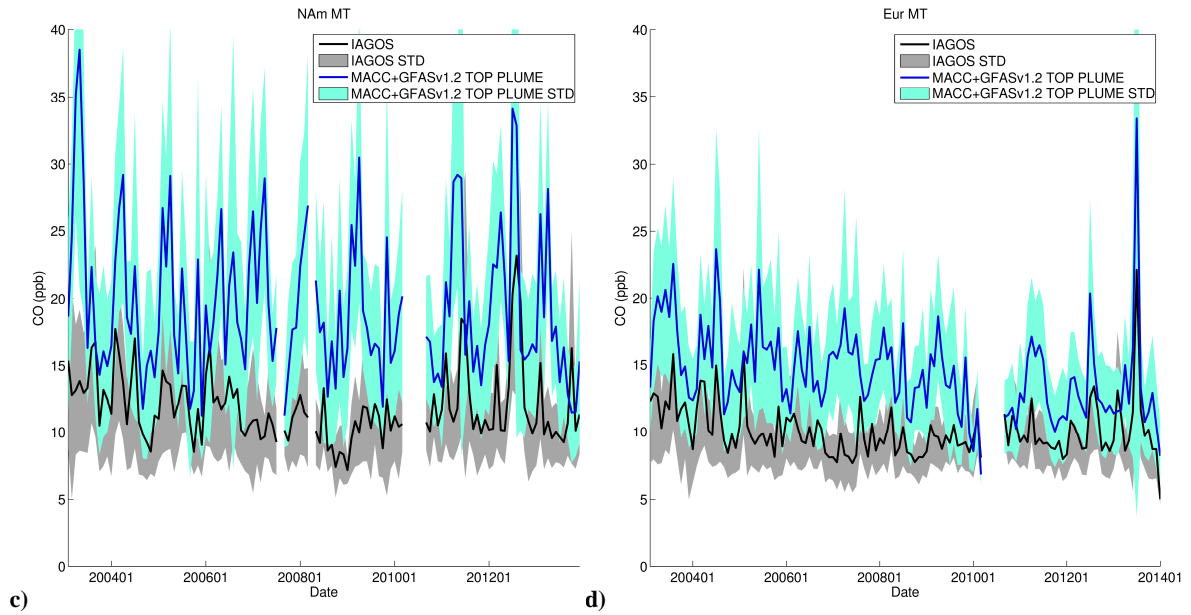
1139 c)

Figure 10: (a) Mean bias (blue) and mean standard deviation bias (black) between the modeled and observed CO anomalies ; (b) Percentiles of the modeled CO anomalies bias with respect to observations; (c) Relative contribution from anthropogenic and biomass burning sources to the modeled CO. The three graphs are for the main sampled regions (Europe, North America, North Atlantic, North Asia, Central Asia, South America, Africa, South Asia) and in three layers (LT, MT, UT), using MACCity and GFASv1.2 for the 2003-2013 period. Biomass burning vertical injection uses APT methodology.

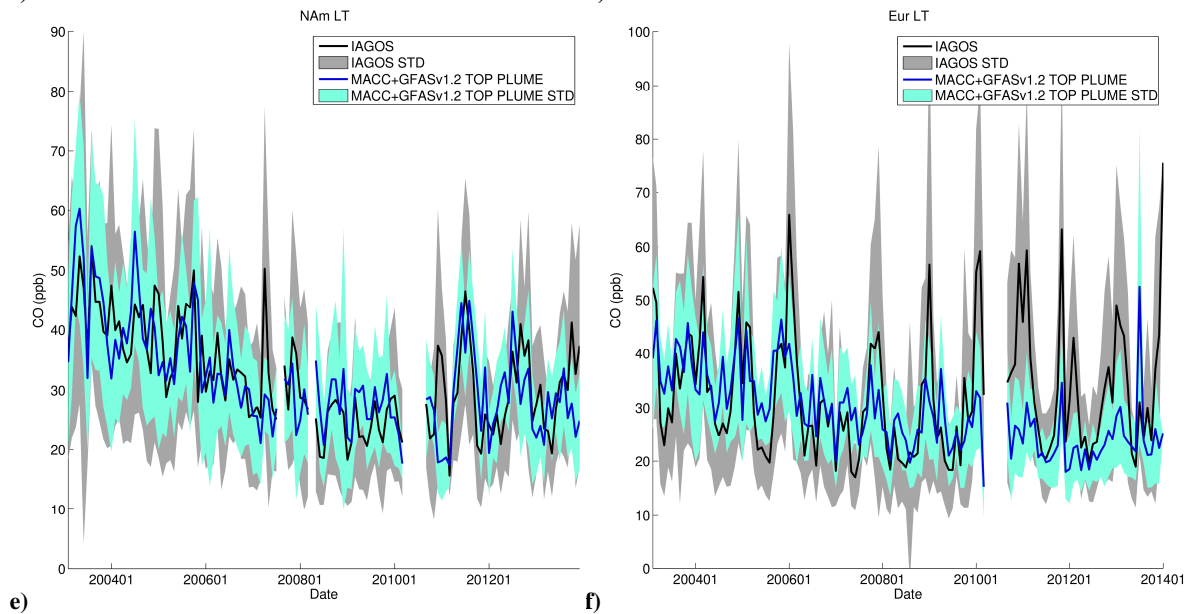
1146



1147



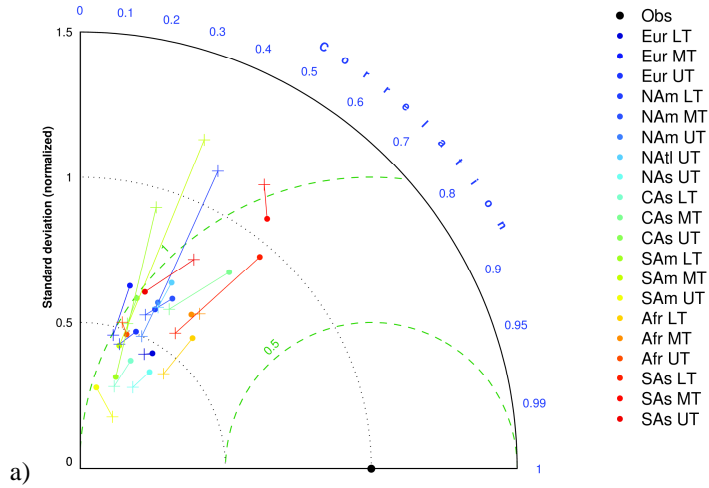
1148



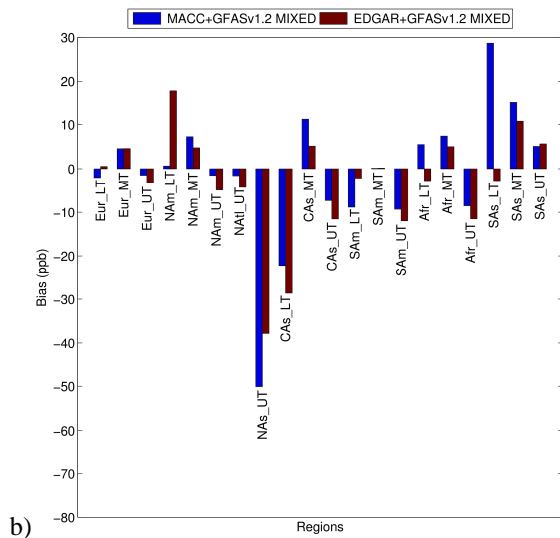
1149 **Figure 11: Times series (monthly means between 2003 and 2013) of the observed (black) and simulated (blue) plumes**
1150 **of CO enhancements for the two most documented regions (North America and Europe) in the LT (e & f), MT (c & d)**
1151 **and UT (a & b), using MACCity and GFASv1.2. Standard deviations are in gray (observations) and light blue (SOFT-**
1152 **IO). Biomass burning vertical injection uses APT methodology.**

1153
1154
1155
1156
1157
1158
1159
1160
1161
1162
1163
1164
1165
1166
1167
1168
1169
1170
1171
1172
1173
1174
1175
1176
1177
1178

1179



1180



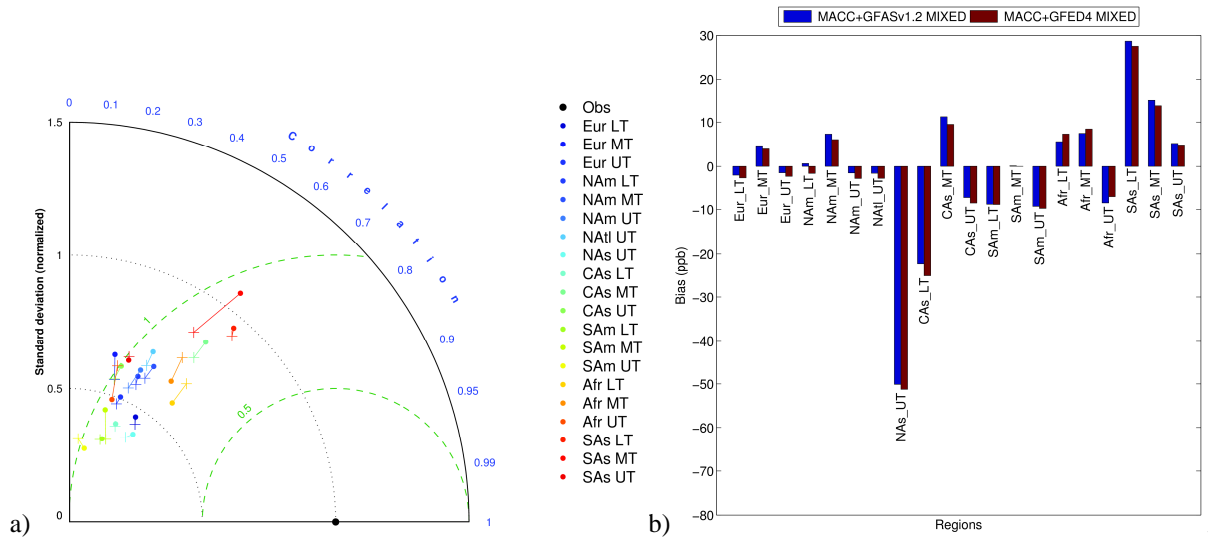
1181

1182

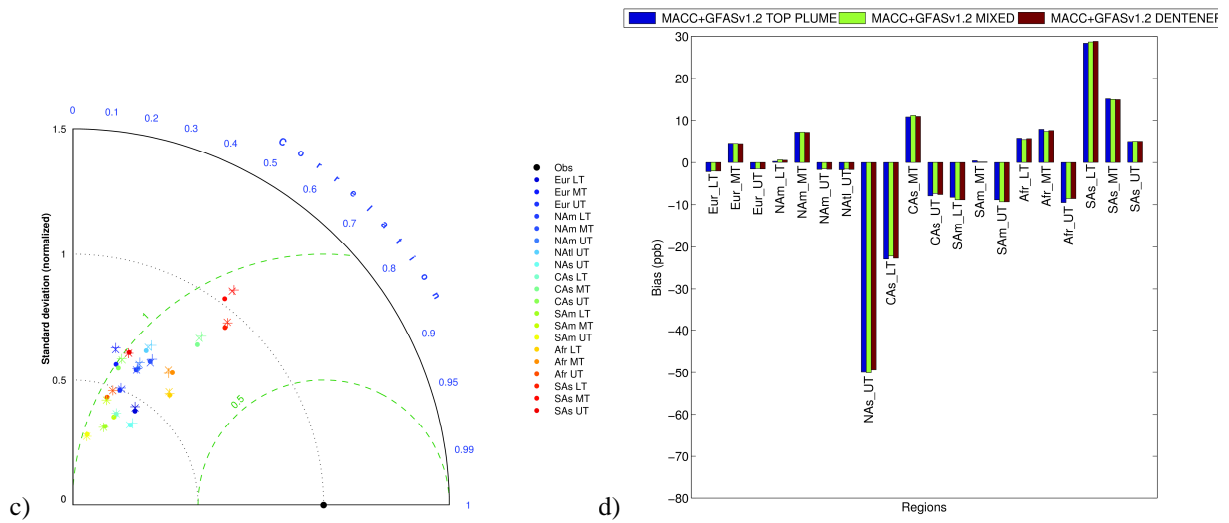
1183 **Figure 12: Comparison of the SOFT-IO anthropogenic emission influence between 2002 and 2008 (a) Taylor diagrams**
 1184 **are obtained for the different regions and in the three vertical layers (LT, MT and UT) using MACCcity (dots) and**
 1185 **EDGARv4.2 (crosses) with GFAS (lines represent connexions between the two inventories) (b) Mean biases between**
 1186 **the modelled (blue for MACCcity + GFAS; brown for EDGARv4.2 + GFAS) and observed CO anomalies. The MIXED**
 1187 **methodology is used for fire vertical injection**

1188

1189
1190



1191



1192

1193 **Figure 13: Comparison of the SOFT-IO biomass burning emission influence between 2003 and 2013. Taylor diagrams**
 1194 **are obtained for the different regions and in the three vertical layers (LT, MT and UT) using (a) GFASv1.2 (dots) and**
 1195 **GFED4 (crosses) with MACCcity and MIXED methodology for both GFASv1.2 and GFED4 (lines represent**
 1196 **connexions between the two inventories); (c) GFASv1.2 and MACCcity with different vertical fire injections**
 1197 **methodologies: MIXED (dots), APT (plus) and DENTENER (crosses) (lines represent connexions between the two**
 1198 **inventories). Mean biases between modeled and observed CO anomalies. Model is using (b) GFASv1.2 + MACCcity**
 1199 **(blue); GFED4 + MACCcity (brown) and MIXED methodology for both GFASv1.2 and GFED4; (d) GFASv1.2 +**
 1200 **MACCcity and different vertical fire injections methodologies: MIXED (blue); APT (green) and DENTENER (brown)**

1201

1202

1203

1204

1205

1206

1207